Spring 5-5-2023

Hybrid Power Spectral and Wavelet Image Roughness Analysis

Basel White
University of Maine, basel.white@maine.edu

Recommended Citation

HYBRID POWER SPECTRAL AND WAVELET IMAGE ROUGHNESS ANALYSIS

By

Basel Gregory White

B.S. The University of Maine 2022

A THESIS

Submitted in Partial Fulfillment of the

Requirements for the Degree of

Master of Science

(in Biomedical Engineering)

The Graduate School

The University of Maine

May 2023

Advisory Committee:

Dr. Andre Khalil, Professor of Biomedical Engineering, Advisor

Dr. Karissa Tilbury, Assistant Professor of Biomedical Engineering

Dr. Brian Toner, Software Engineer at Tyler Technologies

HYBRID POWER SPECTRAL AND WAVELET IMAGE ROUGHNESS ANALYSIS

By Basel Gregory White

Thesis Advisor: Dr. Andre Khalil

The Two-Dimensional Wavelet Transform Modulus Maxima (2D WTMM) sliding window methodology has proven to be a robust approach, in particular for the extraction of the Hurst (H) roughness exponent from grayscale mammograms. The power spectrum is a computational analysis based on the Fourier transform that can be used to estimate the roughness of a scale-invariant image or region via the calculation of H. We aim to examine how the calculation of H in fractional Brownian motion (fBm) images and mammograms can be improved. fBm images are generated for $H_{theo} \in [0.00, 1.00]$ for testing through the previous 2D WTMM sliding window analysis using the Gaussian smoothing function, the second-order derivative of the Gaussian smoothing function, the Mexican hat, and the power spectrum analysis. The power spectrum is shown to provide a more accurate calculation of H for $H_{theo} < 0.45$ ($RMSE = 0.01$), while the 2D WTMM analysis with the Mexican hat smoothing function provides this for $H_{theo} \geq 0.45$ ($RMSE = 0.058$) in fBm images. Through the previous implementation of the 2D WTMM sliding window analysis, we have categorized mammographic subregions into three categories: Fatty ($H < 0.45$), risky dense ($0.45 \leq H \leq 0.55$), and healthy dense mammographic tissue ($H > 0.55$). The power spectrum and the 2D WTMM analysis are further tested on the CompuMAINE Laboratory's acquired de-identified Perm and Maine mammographic datasets. From this

analysis, it can be concluded that the power spectrum analysis cannot accurately distinguish fatty from dense tissue in grayscale mammograms. The implementation of the Mexican hat smoothing function provides a decrease in the number of mammographic subregions rejected during our analysis. In addition, the Mexican hat smoothing function indicates a greater difference in risky dense mammographic tissue between cancerous and normal patients compared to the previously adapted 2D WTMM analysis with the Gaussian smoothing function. The presence of noise in the Perm mammographic dataset indicates a larger minimum size for the range of wavelet scales a ($MinADelta = 3.0$) should be used in the calculation of H using the Mexican hat smoothing function in the 2D WTMM sliding window analysis. Higher quality (16-bit) mammograms in the Maine mammographic dataset indicate a similar minimum range of wavelet scales used in previous studies ($MinADelta = 1.0$) should be used to calculate H with the Mexican hat smoothing function. Through extensive calibration and testing of the power spectrum and 2D WTMM methodologies, we conclude the implementation of the 2D WTMM methodology with the Mexican hat smoothing function provides the most accurate calculation of $H \in [0.00, 1.00]$ in fBm and mammographic images.

PREFACE

To preface, we acknowledge the Mexican hat wavelet discussed in this thesis is also referred to as the Ricker wavelet. Due to use in previous published papers by the CompuMAINE laboratory, we refer to it as the Mexican hat wavelet and smoothing function throughout this work.

ACKNOWLEDGEMENTS

TABLE OF CONTENTS

LIST OF TABLES

LIST OF FIGURES

CHAPTER 1

INTRODUCTION

Breast cancer is the most common cancer amongst women, occurring in every one in eight [1]. Major research efforts are centered around developing methodologies to improve early detection from mammographic screenings. The Computational Modeling, Analysis of Imagery and Numerical Experiments (CompuMAINE) Laboratory is a University of Maine based laboratory developing and utilizing image and signal processing methods to conquer real-world problems.

The innate heterogeneity of the mammographic tumor environment makes it difficult for researchers to quantify changes in a patient's breast tissue. Changes in the stromal tissue, composed of adipocytes, fibroblasts, blood vessels, etc., and immune cells in the mammographic microenvironment are key in the visual appearance of the tissue through imaging. With this, mammographic density represents the proportion of fibroglandular to adipose tissue in the breast. High mammographic density is associated with more fibroglandular rather than adipose tissue. Mammographic density decreases the overall sensitivity of screening mammography allowing for a potential late-stage diagnosis of breast cancer and thus represents one of the more important breast cancer risk factors, as women with approximately 75 to 100 percent dense breast tissue are at a 4-to-6-fold risk of developing breast cancer [2, 3].

When a screening mammogram is ordered, the patient's breast is imaged in two views: craniocaudal (CC) and mediolateral oblique (MLO). The CC mammographic view is the most common view and images the breast from the top-down, allowing for glandular tissue to be seen. Additionally, the MLO mammographic view allows the radiologist to see the breast tissue present, and a portion of the pectoralis major. If the pectoralis major is not shown, the mammogram is discarded, and the patient is re-imaged from the MLO point of view. Pressure is applied to the chest wall, and the breast is imaged 30-60 degrees to

acquire the MLO view [4]. The screening mammography guidelines are enforced by the American College of Radiology, which recommends yearly screening for patients 40 years of age or older to aid in early detection of breast cancer [5].

Once the breast is imaged, a visual assessment of the screening mammogram is performed by a radiologist. They will then decide if additional breast imaging through diagnostic mammography is necessary; however, the presence of varying levels of mammographic breast density has caused a low cancer detection yield and a high false positive rate of breast cancer [6]. Fatty breast tissue regions are translucent in the X-ray spectrum and are therefore portrayed as dark regions in the mammogram. Epithelial and stromal tissues absorb these X-rays causing them to be portrayed as white on the mammogram (Figure 1.1 A1,2), while tumorous regions xalso appear white (Figure 1.1 B1,2). The elevated presence of epithelial and stromal tissues can obscure cancerous regions in the patient's mammogram leading to high false positive rates (Figure 1.1 B1,2).

In addition, these high false positive rates create unnecessary emotional strain on patients and increase the financial burden due to unneeded biopsies and medical visits [6]. With this, the introduction of clinical support systems, such as computer aided detection (CADe), diagnosis (CADx), and triage (CADt), to the medical field has quite rapidly become valuable tools for radiologists. For breast cancer specifically, CADx and CADe provide a radiologist additional information to aid in their diagnosis. CADt assists a radiologist in prioritizing their patient triage. An example of this is seen through CureMetrix's CADt system designed to push suspicious studies to the top of the work list while also increasing the rate of recall for suspicious cases [7]. One study reported in 2016 that CADe was used in approximately 92% of screening mammograms in the United States [8].

Previous studies have shown that the two-dimensional Wavelet Transform Modulus Maxima (2D WTMM) multi-fractal method is a robust approach for the quantification of density fluctuations in the mammographic microenvironment. In these studies, density
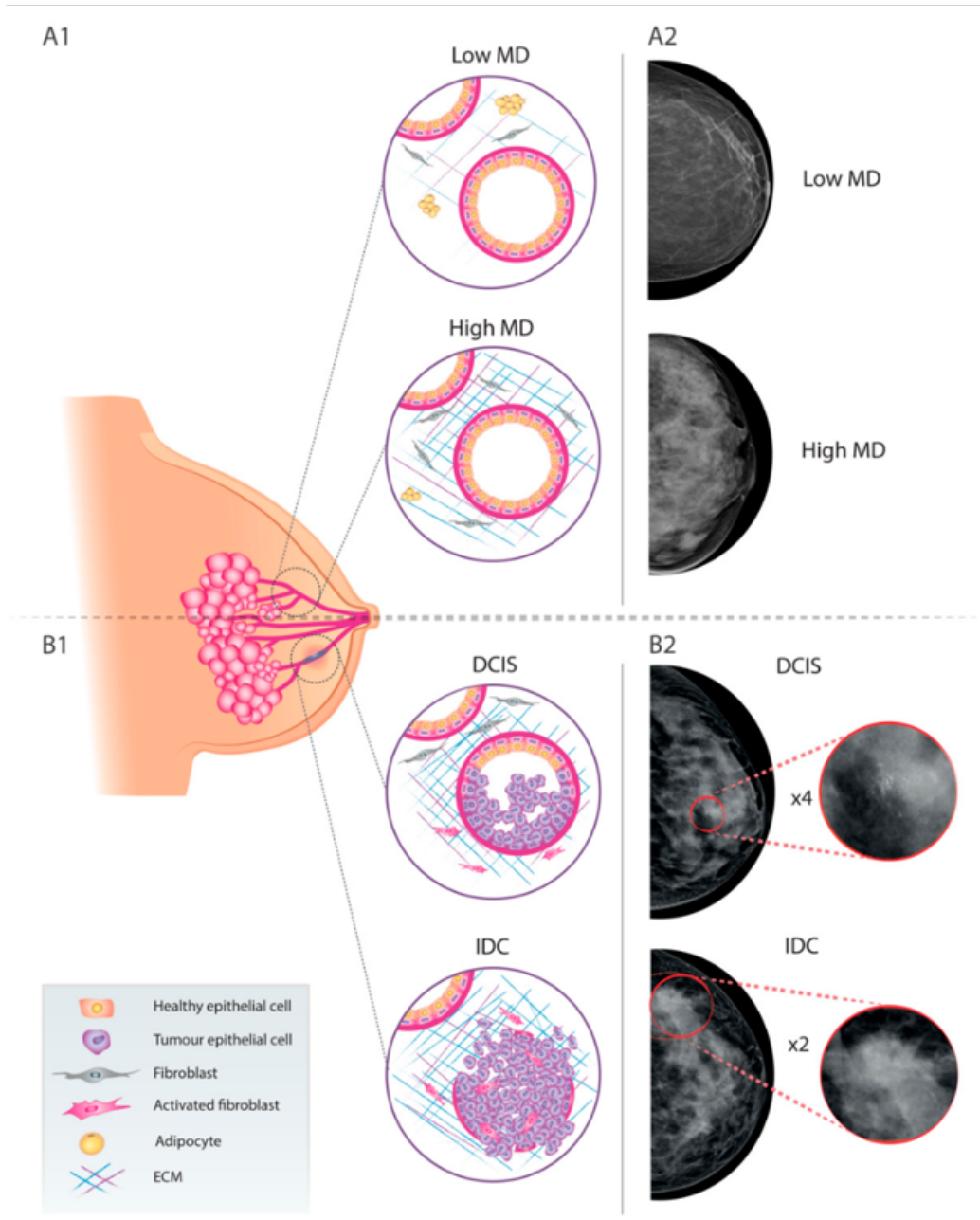
Figure 1.1: Fatty tissue is relatively translucent, since it absorbs few X-rays. Thus, it results in dark areas on the image. Epithelial and stromal tissues filter X-rays more efficiently, absorbing their energy and thus appearing as clear areas (Figure 1 A1, A2). Breast lesions are not easily discernible in these areas since dense tissue and tumors both appear as white areas on a screening mammogram (Figure 1 B1, B2) (Figure reproduced from Ref. [3]).

fluctuations were classified into three categories. In areas of fatty tissue these density fluctuations are monofractal anti-correlated (MAC) ($H < 0.45$), while both monofractal uncorrelated and long-range correlated (LRC) ($H > 0.45$) are seen in dense breast tissue

regions [9, 10]. For dense tissue regions, a H close to 0.5, i.e. $0.45 < H < 0.55$, is associated with the loss of homeostasis and may indicate a proclivity towards developing malignancy in these coined "risky" dense breast tissue regions [9, 10]. This thesis aims to explore the implementation of a power spectral approach through the use of the 2D Fast-Fourier transform in which H can be extracted from the transformed power spectral signal [11]. In addition, the Mexican hat wavelet is the second derivative of the current used Gaussian smoothing. We explore the implementation of the Mexican hat in the 2D WTMM methodology [12]. The higher wavelet order of the Mexican hat wavelet ($n_\psi = 3$) is hypothesized to provide a more robust calculation of H using the 2D WTMM method. Both methodologies are tested on fractional Brownian motion images, with known H, and various patient mammographic datasets. This approach will allow us to discover the most efficient methodology in terms of speed and, most importantly, diagnostic accuracy of H in grayscale mammograms.

CHAPTER 2

LITERATURE REVIEW

2.1 Breast Cancer Risk Assessment

Globally, breast cancer impacts approximately 300,000 women each year with an incident rate between 8.3% and 12.5% [13, 14, 15]. Based on data collected from the SEER Cancer Statistics Review across 2017 to 2019, a women's 10 to 20 year risk of developing breast increases with age (Figure 2.1). With this, it is important to be able to accurately assess a patient's risk at their last regular screening, but also in a longitudinal manner. To accomplish this, there is an ongoing effort to develop breast cancer risk assessment models.
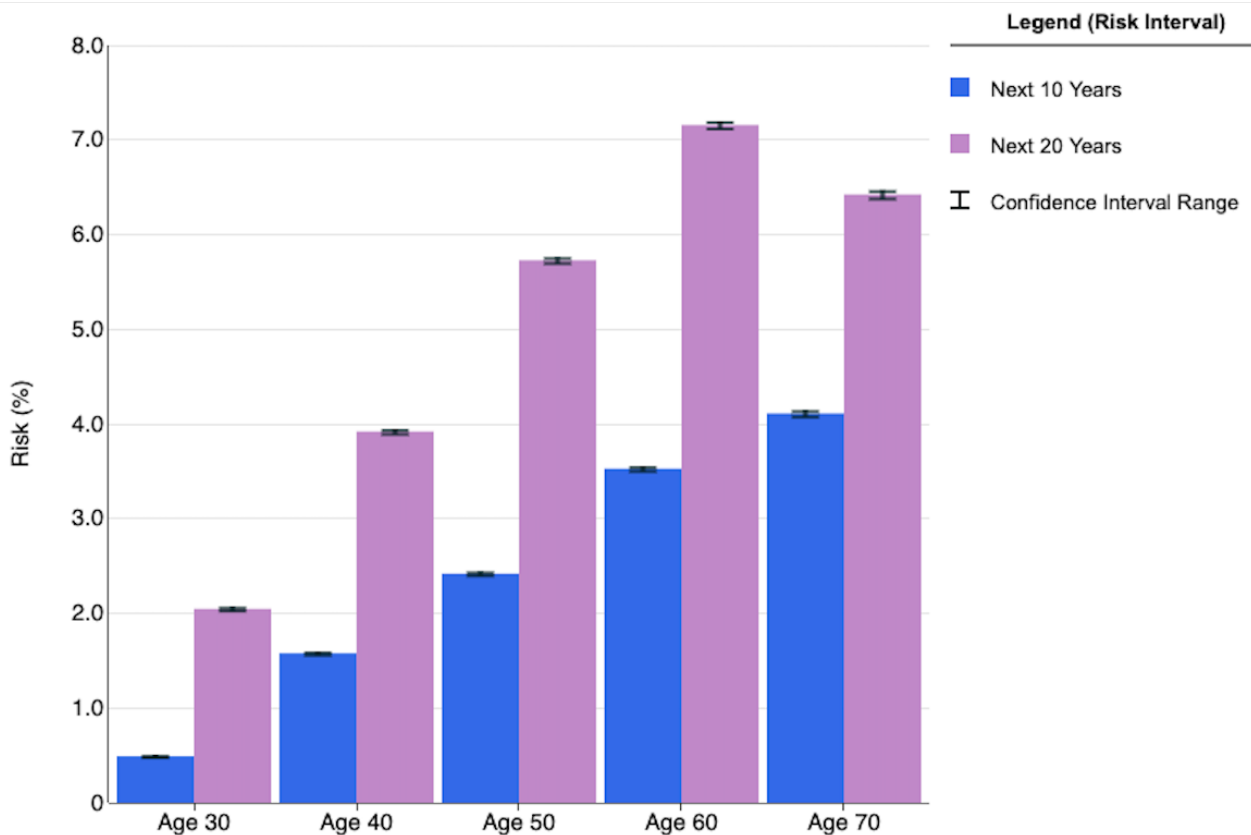
Figure 2.1: According to data collected from the SEER Cancer Statistics Review 2017-2019, a woman's risk of developing breast cancer can be seen to increase with age.

In general, there are two main categories of breast cancer risk assessment models. The first category are models designed to estimate a patient's risk of developing breast cancer [15]. The performance of these models are evaluated through the concordance (c) statistic and observed to expected (O:E) ratio. The c-statistic represents the fraction of data that behaves as expected where a value of 1.0 represents a near perfect discrimination. The O:E ratio represents the actual number of cases versus that of the predicted in the population used for model evaluation [15]. The most commonly used method to assess a patient's risk of developing breast cancer is the Gail model, also known as the Breast Cancer Risk Assessment Tool from the National Cancer Institute, first developed in 1989 [16]. The Gail model focuses on assessing a patient's breast cancer risk with the use of the multivariate linear regression models designed to incorporate various breast cancer risk factors, such as age of menarche and first live birth, number of prior breast biopsies, and recognition of hereditary risk. While the Gail model is one of the oldest and most commonly used risk assessment models its effectiveness has been put into question due to its weakness in high-risk clinical populations (c-statistic: 0.56, O:E ratio: 1.08) [17, 18].

Mammographic density (MD) is one of the most important radiological risk factors for breast cancer assessment, as it is responsible for the formation of dense breast tissue. The clinically accepted manner to assess a patient's MD is through the breast imaging reporting and data systems (BI-RADS) [19, 20]. The BI-RADS system separates a patient's MD into four categories (Figure 2.2):

1. Almost entirely fatty tissue (5-24% MD)

2. Scattered areas of density (25-49% MD)

3. Heterogeneous density (50-75% MD)

4. Extremely dense (MD $\geq$ 75% tissue density).

BI-RADS categories one and four are associated with 10% of women in the U.S., while categories two and three are seen in 40% of women [19]. A 2007 study concluded the

greatest MD is seen in Asian women, while the lowest is seen in African American women [21]. Given the results of this study, the Chen and Tice models extended the Gail model by putting a focus on MD [22, 23]. The Chen model incorporates the average percent breast density from both CC mammograms of the respective patient [22]. Incorporating percent density as a risk factor increases the c-statistic from the Gail model from 0.56 to 0.64 [22]. Rather than incorporating percent density, the Tice model incorporates BI-RADS density classifications to predict the 5-year risk of invasive breast cancer in women not diagnosed with breast cancer. Validation results from the Tice model demonstrate low discrimination (c-statistic: 0.66) and high calibration (O:E: 1.03). Additionally, the Tice model's lack of family history and incorporation of BI-RADS categories for MD demonstrates it should be interpreted with caution [23]. With this, the Chen model's elevated discrimination and
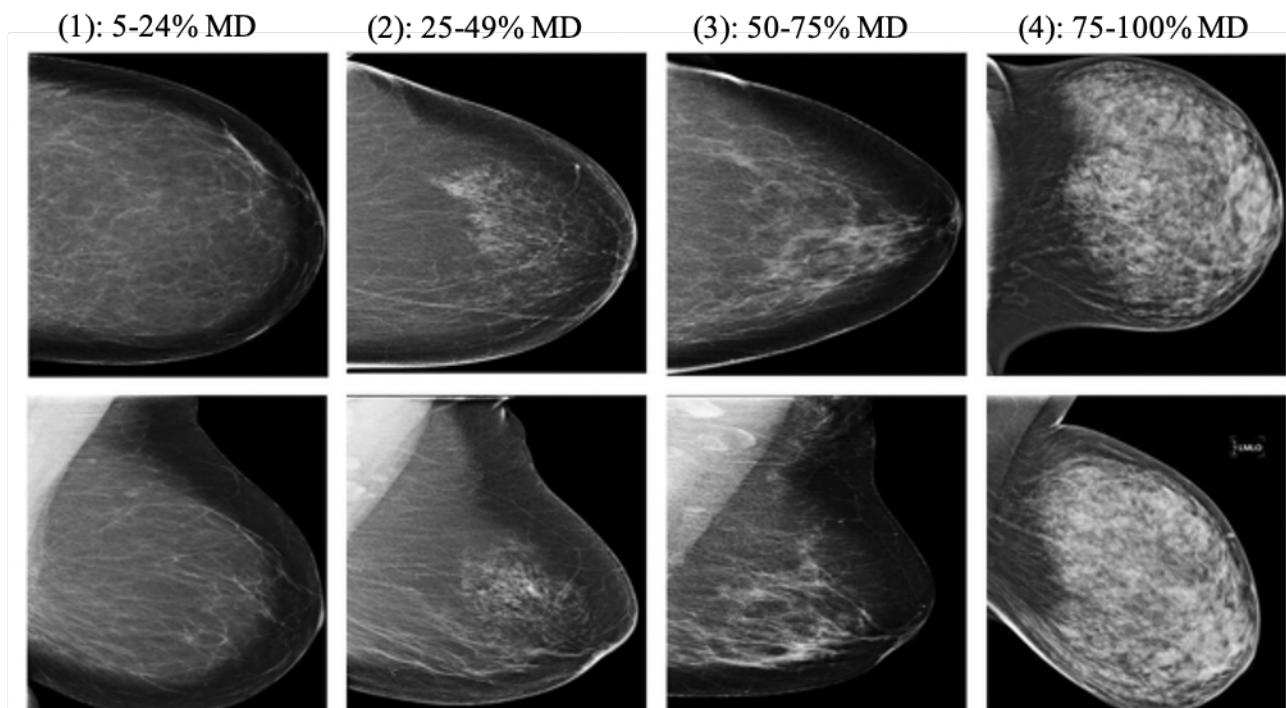
Figure 2.2: Clinically, the assessment of breast density is accomplished through the use of the Breast Imaging Reporting and Data System (BIRADS) [20]. This system is broken down into four categories: **(1)** almost entirely fatty (5-24% MD), **(2)** scattered areas of fibroglandular density (25-49% MD), **(3)** heterogeneously dense (50-75% MD), and **(4)** extremely dense breast tissue (75-100% MD).

incorporation of additional breast cancer risk factors, in comparison with the Gail model, would grant a radiologist insight into accurately assessing a patient's breast cancer risk.

The second category of breast cancer risk assessment models are those designed to estimate a patient's risk of carrying a high-risk genetic mutation. The Myriad model, developed in 1997, was the first risk assessment model designed to predict a patient's genetic carrier status of the $BRCA1$ mutation [24]. This model is only for patients deemed high-risk due to their respective family history and was validated on 798 women with high-risk history and no current documentation of genetic mutations. Logistic regression was utilized to determine the breast cancer risk factors applicable for the $BRCA1$ mutation [24]. In 1998, Frank et al. accounted for the $BRCA2$ mutation by applying logistic regression to estimate the probability of carrying the $BRCA1$ or $BRCA2$ mutation through assessing the patient's family history [25]. A group of 10,000 women were genetically tested to determine their risk of possessing the $BRCA1$ or $BRCA2$ mutation. The Myriad II model was tested on this group of women. Validation results of the Myriad II's ability to predict $BRCA$ carrier status was performed through the use of sensitivity and specificity reporting 0.71 and 0.63, respectively [25]. Upon validating the model, it was discovered that the Myriad II model demonstrated an underrepresentation for the Korean and southern Chinese populations and an overall underestimation for patients with a limited family history [26].

In addition to the Myriad II, another commonly used model is the Couch or UPenn model. This model, which was developed in 1997, was intended for patients with a family history of breast cancer and is used to estimate the patient's risk of developing a $BRCA1$ mutation. Further, it is also used to estimate the patient's family member's risk. The model accounts for risk of developing breast and ovarian cancer, and the average age of diagnosis for both. The Couch model was validated through a logistic regression analysis of 263 families with a family history of breast cancer and with or without a history of ovarian cancer. The Couch model is commonly used in the clinical setting due to its ease of use

and incorporation of accessible clinical data [27]. Rather than assessing a patient's risk of carrying a $BRCA$ germline mutation, the family history assessment tool (FHAT) is an algorithm implemented to aid clinicians in their assessment of a patient's need for genetic counseling [28]. FHAT assigns points to the relationship of the affected individual, age of onset, and the type and number of primary cancers. The total points are calculated for an overall family FHAT score. Each family member who has been diagnosed with breast, ovarian, colon, or prostate cancer is scored individually. The FHAT algorithm was validated using 184 families from the Ontario Familial Breast Cancer Registry [28]. Similar to the Myriad II model, validation of the FHAT algorithm was performed through the use of sensitivity and specificity reporting 0.94 and 0.51, respectively. FHAT validation results demonstrates its ability to identify high-risk patients for further evaluation through incorporation of family history [28].

Rather than assessing a patient's risk of developing breast cancer or a germline mutation individually, more effective models have considered both of these risk factors into their assessment. The BRCAPRO model was initially introduced in 1997 to predict $BRCA$1 and $BRCA$2 mutations, assess a patient's risk to develop invasive breast or ovarian cancer, or develop contralateral breast cancer [29, 30]. BRCAPRO can be applied to patients with or without a family history of breast or ovarian cancer. Similar to BRCAPRO, the Breast and Ovarian Analysis of Disease Incidence and Carrier Estimation Analysis (BOADICEA) was first described in 2002 and refined in 2004 to calculate the probability of the $BRCA$1 and $BRCA$2 mutations in the respective patient, while also assessing the risk of breast and ovarian cancer development [31, 32]. With an update in 2014, the BOADICEA model was extended to incorporate family history of male breast, prostate, pancreatic cancer, and tumor pathology into its risk factors [31, 32, 33].

Finally, the Internal Breast Cancer Study Breast Cancer Risk Evaluation Tool, known as the Tyrer-Cuzick (TC) model, has the same goal as the BRCAPRO and BOADICEA models [34]. The TC model incorporates a wide variety of risk factors, demonstrates better

calibration and predictive accuracy than the Gail model, and tends to calculate a higher lifetime risk than the BRCAPRO model [35]. The TC model is also the only one out of the three combined risk assessment models to incorporate mammographic density as a risk factors (Table 2.1) [36, 37]. Overall, the Gail model is the most commonly used risk assessment model in the clinical setting. However, the problems seen in this model has caused for image-based risk assessment to be implemented to assess a patient's risk of developing breast cancer. With this, iCAD has recently developed the ProfoundAI image-based breast cancer risk assessment technology. ProfoundAI provides a one to three year breast cancer risk estimation from a patient's 2D or 3D mammogram through incorporating age, breast density, and mammographic features [38, 39].

Table 2.1: A comparison of risk factors for various clinically implemented breast cancer risk assessment models. The Tyrer-Cuzick model is continually updated and is one of the few risk assessment models to incorporate mammographic density and additional breast cancer risk factors.

Risk Factors	Hormonal Models			Hereditary Models					
	Gail	Chen	Tice	Myriad	Couch	FHAT*	BRCAPRO	BOADICEA†	Tyrer-Cuzick
Age	X			X			X	X	X
Age of Menarche	X								X
Age of First Live Birth	X	X							X
Age of Menopause									X
Number of biopsies	X	X	X						X
History of Atypical Hyperplasia	X	X							X
Number of first-degree relatives with BC	X								
Breast Density		X	X						X
BMI		X							
Race / Ethnicity			X	X	X		X		X
Other					X		X	X	X

* Family History Assessment Tool (FHAT)

† Breast and Ovarian Analysis of Disease Incidence and Carrier Estimation Algorithm (BOADICEA)

CHAPTER 3

FRACTIONAL BROWNIAN MOTION IMAGES

3.1 Fractional Brownian Motion Image Generation

The fractional Brownian motion (fBm) image concept was first introduced by
Mandelbrot and Ness [40]. fBm images are generated with a known Hurst exponent (H) in
which all points throughout the image possess the same roughness, i.e. with a monofractal
signature. The generation of these images has become an area of interest to study various
image analysis and processing techniques. A two-dimensional fBm image, $B_H(x)$, is
indexed from $H \in [0.00, 1.00]$ is a stationary zero-mean Gaussian process whose correlation
function is defined as

$$< B_H(\boldsymbol{x}) \, B_H(\boldsymbol{y}) > = \frac{\sigma^2}{2} \left(|\boldsymbol{x}|^{2H} + |\boldsymbol{y}|^{2H} - |\boldsymbol{x} - \boldsymbol{y}|^{2H} \right), \tag{3.1}$$

where $< ... >$ represents the ensemble mean value and $\boldsymbol{x}, \boldsymbol{y} \in \boldsymbol{R}^2$ are points in the image
domain [11]. The variance of this process can be shown through

$$Var[B_H(\boldsymbol{x})] = \sigma^2 |\boldsymbol{x}|^{2H}, \tag{3.2}$$

for any $\boldsymbol{x} \in \boldsymbol{R}^2$. For $H = 1/2$, motion in the fBm image is considered to be uncorrelated;
however, for $H > 1/2$, motion is considered to be positively correlated, while if $H < 1/2$,
negative correlation is seen. Through the correlation function (Equation 3.1), one gets

$$B_H(\mathbf{x}_0 + \lambda \mathbf{u}) - B_H(\mathbf{x}_0) \simeq \lambda^H [B_H(\mathbf{x}_0 + \mathbf{u}) - B_H(\mathbf{x}_0)], \tag{3.3}$$

where $\mathbf{u}$ describes a unit vector, $\simeq$ represents the equality in law, and λ represents a
rescaling factor. Equation 3.3 demonstrates that fBm images are a self-affine process. The
higher the value of H the more regular the motion. For any $\mathbf{x}_0$ in any direction $\mathbf{u}$, the fBm
image is continuous and non-differentiable characterized by the Hölder exponent,
$h(\mathbf{x_0}) = H$ (Equation 3.3). The fBm image can further be described by a singularity

spectrum, $D(h)$, reducing to one point, thus indicating the fractal dimension, D, of the points in the domain of the image shown through

$$D(h) = \begin{cases} 2, & h = H. \\ -\infty, & h \neq H, \end{cases} \tag{3.4}$$

in which $h = H$ is equal to 2. The CompuMAINE Laboratory possesses an in-house software called Xsmurf consisting of approximately 130,000 lines of C and Tcl code. An existing Xsmurf function *ibro* allows for fBm images of a specific size and H to be generated using the Fourier transform filtering synthesis method [41]. In order to have a sufficient sample size for testing, 500 fBm calibration images were generated for each H ranging from 0 to 1 in 0.05 increments. Figure 3.1 demonstrates three of these fBm images for $H = 0.25$ (a), $H = 0.50$ (b), and $H = 0.75$ (c) with their corresponding surface plots in gray, red, and cyan, respectively.
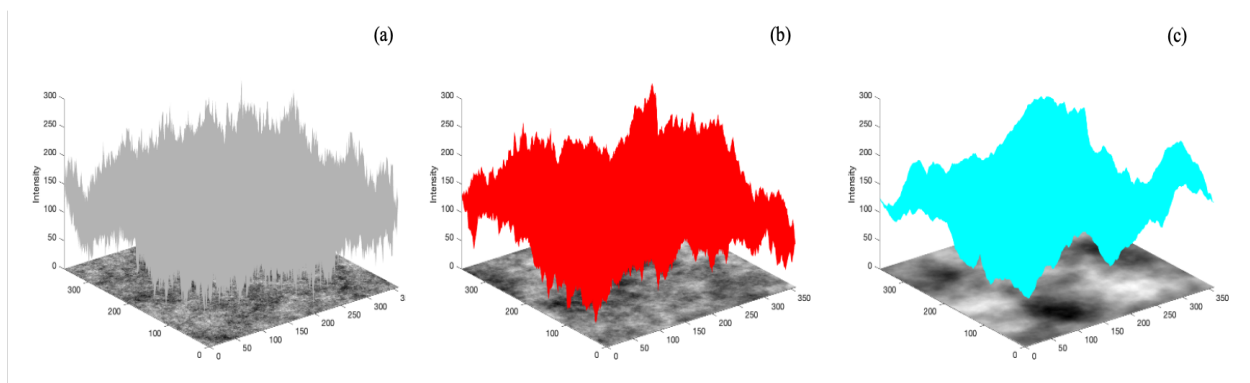
Figure 3.1: fractional Brownian motion (fBm) images are often used as testing images. fBm images of size 360 by 360 pixels with known Hurst (H) exponent and their surface plots: $H = 0.00$ (gray), $H = 0.50$ (red), and $H = 1.00$ (cyan).

CHAPTER 4

METHODS

4.1 The Two-Dimensional Wavelet Transform Modulus Maxima Methodology

The Two-Dimensional Wavelet Transform Modulus Maxima (2D WTMM) multi-fractal method has proven to be a robust approach in analyzing the mammographic microenvironment [9, 10, 42]. The 2D WTMM methodology allows for a wavelet transform (WT) to be implemented as a mathematical microscope in order to characterize roughness in an image. An image f is convolved with a wavelet $\psi_1(x,y) = \frac{\partial \phi(x,y)}{\partial x}$ and $\psi_2(x,y) = \frac{\partial \phi(x,y)}{\partial y}$, where $\phi(x,y)$ represents the 2D smoothing function [43]. The WT is defined as

$$\mathbf{T}_\psi[f](\mathbf{b}, a) = \begin{pmatrix} T_{\psi_1}[f] = a^{-2} \int \psi_1(a^{-1}(\mathbf{x} - \mathbf{b})) f(\mathbf{x}) \\ T_{\psi_2}[f] = a^{-2} \int \psi_2(a^{-1}(\mathbf{x} - \mathbf{b})) f(\mathbf{x}) \end{pmatrix}. \tag{4.1}$$

The Mexican hat smoothing function can be derived from the second derivative of the Gaussian function as shown below

$$\phi_{Gau}(x,y) = e^{-(x^2+y^2)/2} = e^{-|\mathbf{x}|^2/2}$$
$$\phi_{Mex}(\mathbf{x}) = \frac{d^2}{dx^2}(\phi_{Gau}) = (2 - \mathbf{x}^2)e^{-|\mathbf{x}|^2/2}. \tag{4.2}$$

The first-order wavelets ψ_1 and ψ_2 are shown for the Gaussian ϕ_{Gau} (Equation 4.2) and Mexican hat smoothing function ϕ_{Mex} (Equation 4.2) on the top and bottom rows, respectively, in Figure 4.1. The implementation of higher order wavelets, where the number n_ϕ of vanishing moments of ϕ conditions the order of the wavelet, $n_\psi = n_\phi + 1$, allows the WTMM methodology to characterize images with $H > 1$ [12, 43]. The 2D WT (Equation 4.1) can also be written in terms of its modulus and argument defined as

$$\mathbf{T}_\psi[f](\mathbf{b}, a) = (\mathcal{M}_\psi[f](\mathbf{b}, a), \mathcal{A}_\psi[f](\mathbf{b}, a)), \tag{4.3}$$

where

$$\mathcal{M}_\psi\left[f\right](\mathbf{b}, a) = \left[\left(T_{\psi_1}\left[f\right](\mathbf{b}, a)\right)^2 + \left(T_{\psi_2}\left[f\right](\mathbf{b}, a)\right)^2\right]^{\frac{1}{2}} \tag{4.4}$$

$$\mathcal{A}_\psi\left[f\right](\mathbf{b}, a) = Arg\left(T_{\psi_1}\left[f\right](\mathbf{b}, a) + i T_{\psi_2}\left[f\right](\mathbf{b}, a)\right). \tag{4.5}$$

The Wavelet-Transform Modulus Maxima (WTMM) are locations $\mathbf{b}$ where $\mathcal{M}_\psi[f](\mathbf{b}, a)$ is
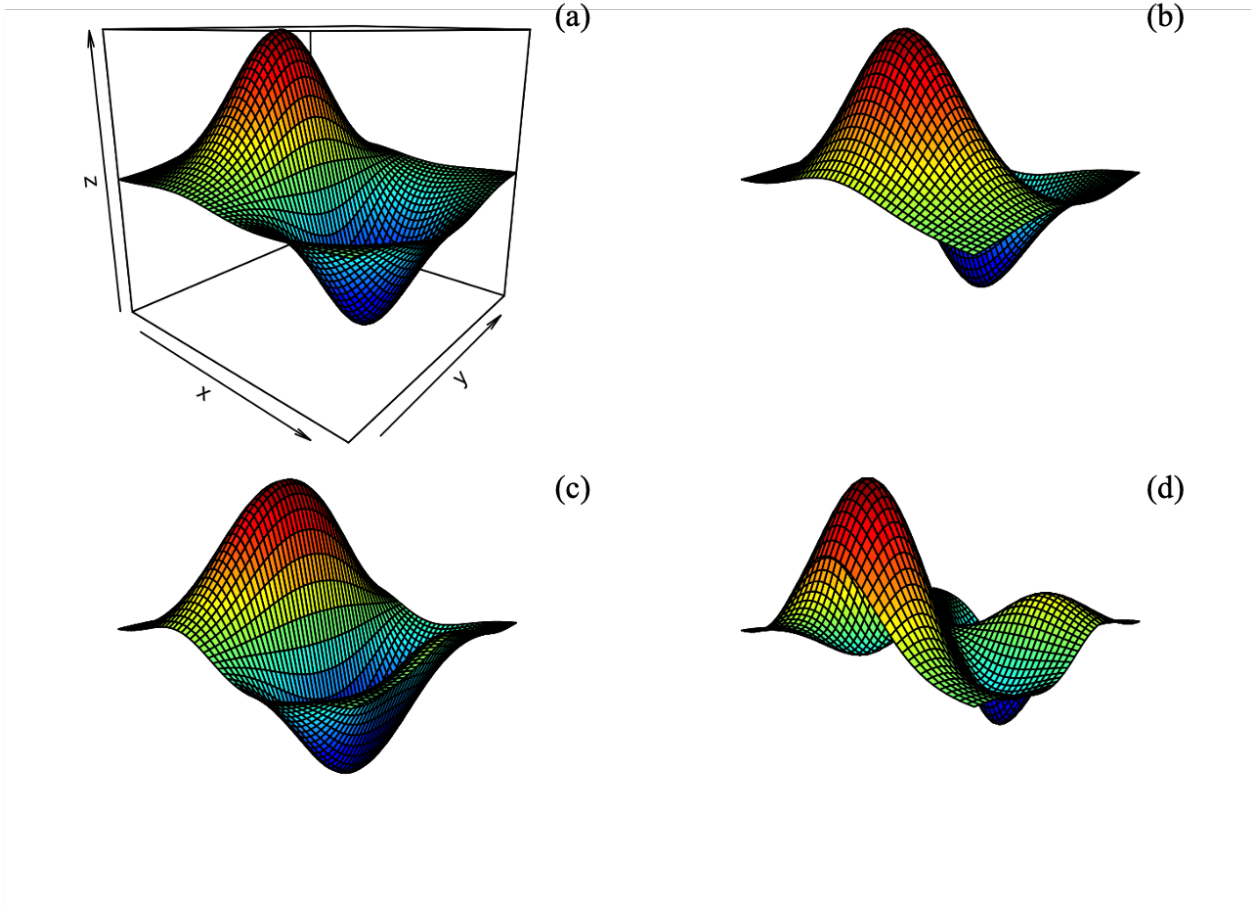
Figure 4.1: The first-order Gaussian smoothing function's ϕ_{Gau} associated wavelets: ψ_1 (a) and ψ_2 (b). The second-order derivative of the Gaussian smoothing function is known as the Mexican hat ϕ_{Mex}. The Mexican hat's associated wavelets: ψ_1 (c) and ψ_2 (d) (Equation 4.2).

a local maximum in the angular direction of $\mathcal{A}_\psi[f](\mathbf{b}, a)$ for wavelet scales a. These

WTMM organize gradient changes of the image into connected chains known as maxima

chains, as shown through the red lines for three different wavelet scales in Figure 4.2

[11, 12, 44]. The black dots on the WTMM chains in Figure 4.2 are the WTMM maxima

(WTMMM). WTMMM are defined as the points along the maxima chains where
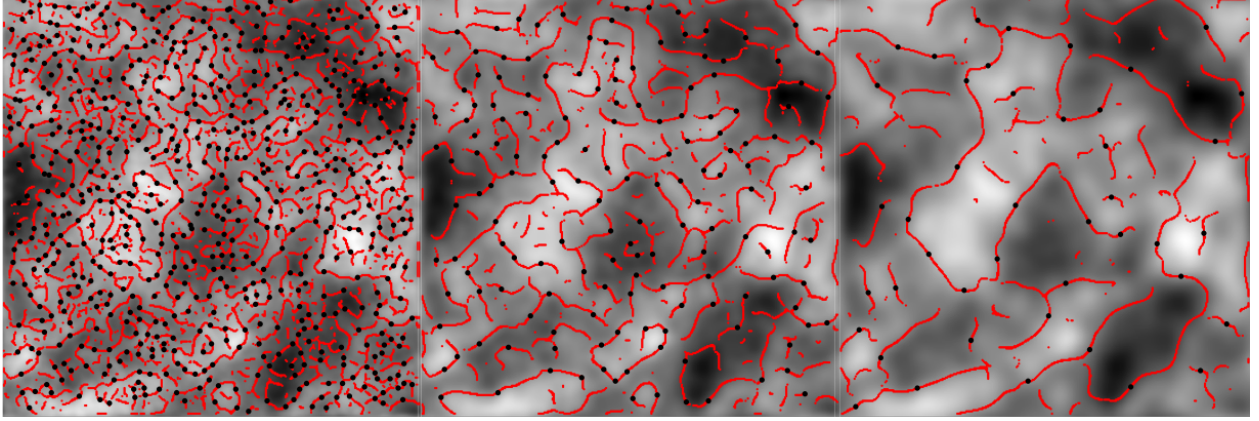
Figure 4.2: The maxima chains are shown for scales $a = 2^1\sigma_w$ (left), $a = 2^2\sigma_w$ (middle), and $a = 2^3\sigma_w$ (right) (where $\sigma_w = 7$ pixels) overlaid onto a 2D fBm image with $H = 0.5$. The local maxima along $\mathcal{M}_\psi$ (WTMMM) are shown through small filled black dots.

$\mathcal{M}_\psi[f](\mathbf{b}, a)$ is locally maximum. Across all wavelet scales a, these WTMMM, from each individual WTMM chains, are connected to form maxima lines. The set of all maxima lines are known as the WT space-scale skeleton $\mathcal{L}(a)$, as shown for the Gaussian and Mexican hat smoothing functions in Figure 4.3abc and Figure 4.3def, respectively. Along a maxima line pointing to the singularity $\mathbf{x_0}$ in the rough surface as $a \to 0^+$, denoted $\mathcal{L}_{\mathbf{x_0}}(a)$, the WTMMM follow [45]

$$\mathcal{M}_\psi[f](\mathcal{L}_{\mathbf{x_0}}(a)) \sim a^{h(\mathbf{x_0})}, \quad a \to 0^+, \tag{4.6}$$

where $h(\mathbf{x_0})$ is the Holder roughness exponent. Equation 4.6 only holds when the wavelet order is greater than the Holder exponent being estimated i.e. when $n_\psi > h(\mathbf{x_0})$. For a set of maxima lines in $\mathcal{L}(a)$, a partition function can be called for wavelet scales a defined as [11, 12, 44]

$$Z(q, a) = \sum_{l \in \mathcal{L}(a)} \left(\sup_{(\mathbf{b}, a') \in l, a' \leq a} \mathcal{M}_\psi[f](\mathbf{b}, a') \right)^q, \tag{4.7}$$

where q are the statistical order moments. Using the information from the partition function, the roughness of a surface can be characterized by the $\tau(q)$ spectrum, obtained from the power-law behavior of the partition function [11]

$$Z(q, a) \sim a^{\tau(q)}, a \to 0^+. \tag{4.8}$$

15
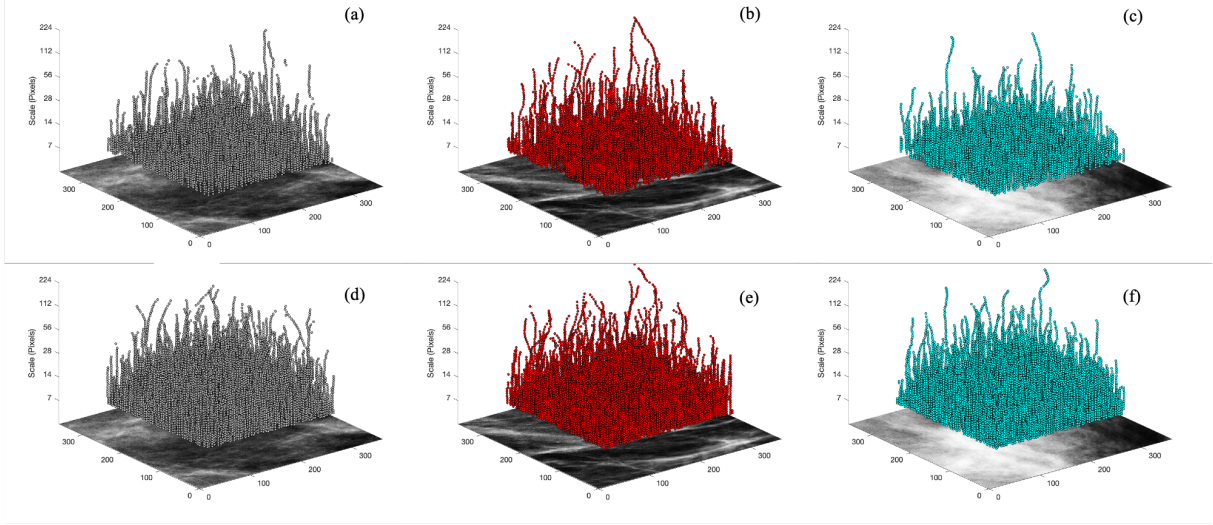
Figure 4.3: Across wavelet scales a, WTMMM (black dots in Figure 4.2) can be connected to form maxima lines. These maxima lines construct the wavelet transform skeleton, $\mathcal{L}(a)$, shown for fatty (ad), risky dense (be), and healthy dense tissue (cf) from the Gaussian (top) and Mexican hat (bottom) smoothing functions.

Given the monofractal nature of fBm images, the $\tau(q)$ spectrum is a linear function of q defined below

$$\tau(q) = qH - 2, \tag{4.9}$$

where the slope of $\tau(q)$ is an estimate of H. Multi-fractal surfaces would cause the $\tau(q)$ spectrum to behave in a non-linear manner [44]. In order to obtain the singularity spectrum, a Legendre transform is applied to $\tau(q)$ spectrum [11, 12, 44]

$$D(h) = \min_{q}(qh - \tau(q)). \tag{4.10}$$

However, to properly investigate the potential numerical uncertainties related to the $D(h)$ calculation, expectation values can be computed through

$$h(q, a) = \sum_{l \in \mathcal{L}(a)} \ln \left| \sup_{(\mathbf{b}, a') \in l, a' \leq a} \mathcal{M}_{\psi}[f](\mathbf{b}, a') \right| W_{\psi}[f](q, l, a) \tag{4.11}$$

and

$$D(q, a) = \sum_{l \in \mathcal{L}(a)} W_{\psi}[f](q, l, a) \ln W_{\psi}[f](q, l, a). \tag{4.12}$$

16

The computation of these expectation values gives

$$h(q) = \frac{d\tau(q)}{dq} = \lim_{a \to 0^+} \frac{h(q, a)}{\ln a} \qquad (4.13)$$

and

$$D(q) = \lim_{a \to 0^+} \frac{D(q, a)}{\ln a} \qquad (4.14)$$

from which we obtain the $D(h)$ singularity spectrum. These calculations are highlighted for three example fBm images of $H = 0.25$ (gray), 0.50 (red), and 0.75 (cyan) using the Gaussian smoothing function (Figure 4.4). The q-values allow one to emphasize different singularity strengths for the analysis of a surface by weighing the modulus of the WT along the maxima lines [12].

4.2 The Power Spectral Analysis

In addition to the 2D WTMM methodology, a power spectral analysis was also explored as a methodology to calculate H in both fBm images and mammograms. H can be extracted from the scaling of the power spectrum signal $S(k)$ expressed as a function of the wavevector ($\mathbf{k}$), where $\mathbf{k} = (k, \theta)$

$$S(k) = \frac{1}{2\pi} \int d\theta |\hat{f}(k, \theta)|^2 \ k^{-\beta}. \qquad (4.15)$$

where k is the spatial frequency and β is the power spectral exponent. Equation 4.15 a power-law relationship $S(k) \sim (1/k)^\beta$ [11]. H is calculated from the power spectrum signal by plotting $\log_2(S(k))$ versus $\log_2(k)$. The slope of the linear portion of the power spectrum signal (-β) is used to calculate H through $\beta = 2H + 2$ (Figure 4.5). β and H are calculated in Xsmurf through the *i2sp* function which requires the image, number of points of the power spectrum signal, and log base for the signal to be transformed to as arguments.

4.3 Additional Methodologies

In addition to the 2D WTMM and power spectral methodologies, differential box counting (DBC) is another methodology for extracting fractal dimension (FD) and H from

17
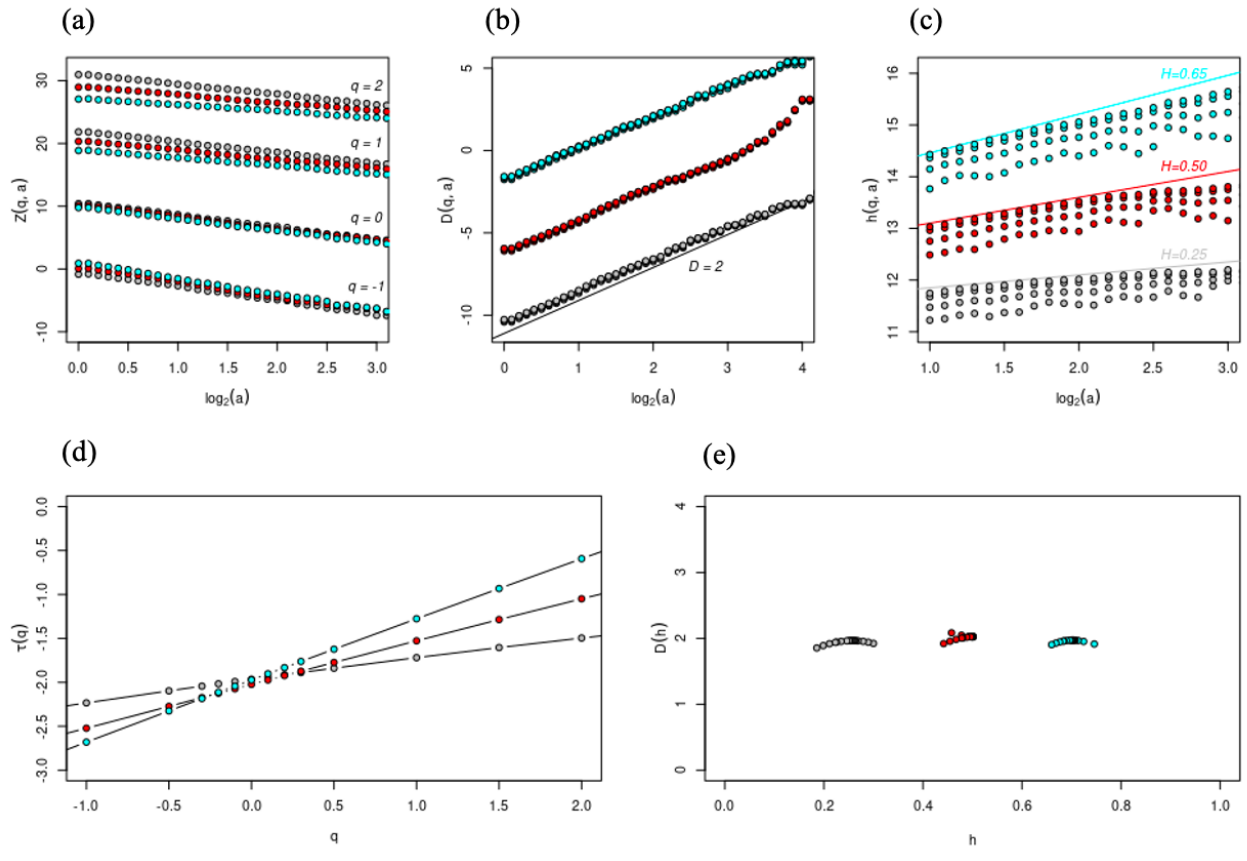
Figure 4.4: 2D WTMM analysis with the Gaussian smoothing function for fBm images of $H = 0.25$ (gray), $H = 0.50$ (red), and $H = 0.75$ (cyan). $Z(q, a)$ (Eq. 4.7), $D(q, a)$ (Eq. 4.12), and $h(q, a)$ (Eq. 4.11) versus $log_2(a)$ for q-values ranging from -1 to 2 (a-c). $\tau(q)$ (Eq. 4.9) versus all q (d). The monofractal nature of the fBm image is demonstrated through the linearity of $\tau(q)$ and clustering of $D(h)$ (Eq. 4.10) (e).

images [46]. DBC allows for the FD of an image to be calculated through $FD = \frac{log(N(r))}{log(1/r)}$, where $N(r)$ is the number of boxes of side length r needed to cover all points in the image [46]. The primary concern with DBC is the inaccuracy of H through over and under counting; however, this methodology is continually being improved [47]. The calculation of H in a self-affine series can be accomplished through various methodologies. The roughness length (RL) methodology implements a sliding window mechanism over a one dimensional (1D) fBm signal. The standard deviation of H is proportional to the sliding window size defined by $R(w) = Aw^H$ where the log-log plot of roughness length $R(w)$ versus sliding window size w allows for the calculation of H [48]. Rescaled range analysis (R/S) divides a

18
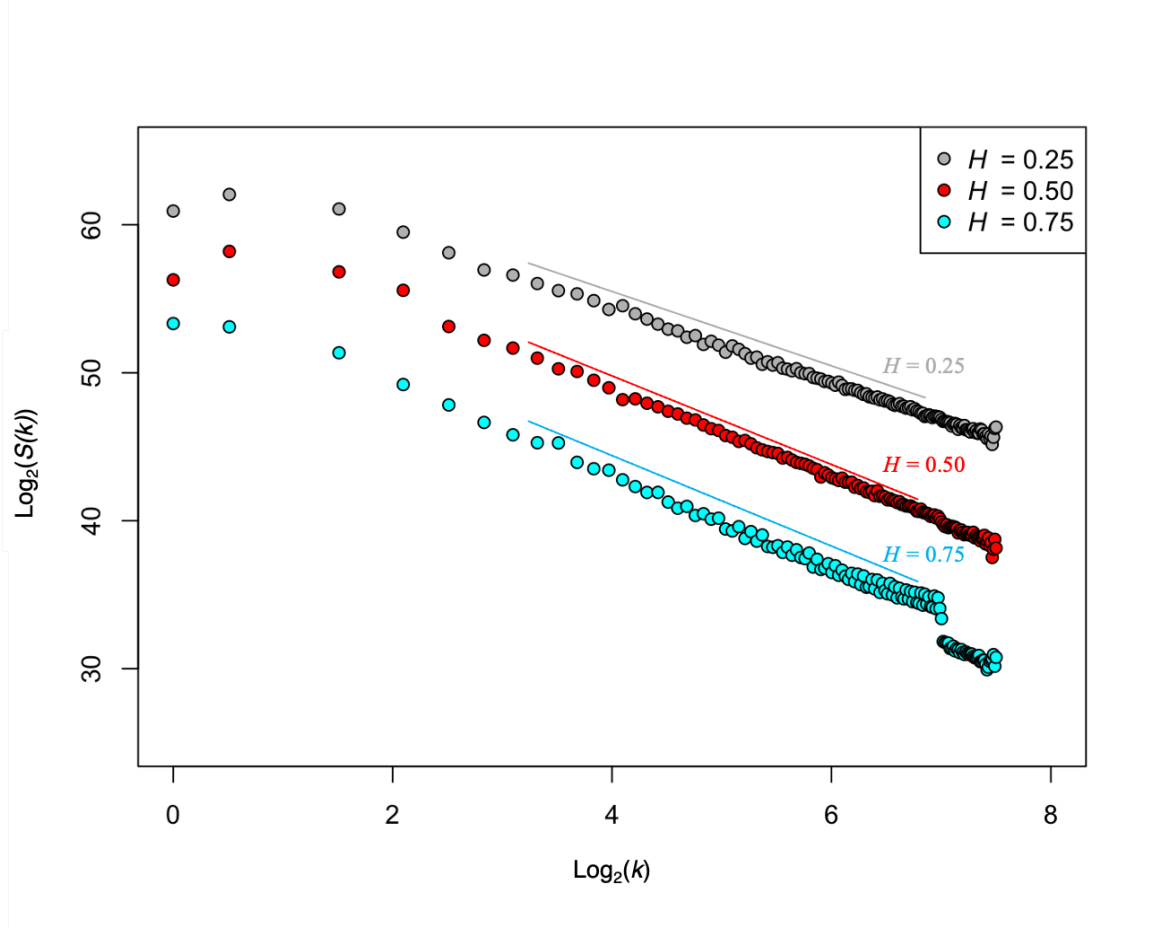
Figure 4.5: For fBm images of $H = 0.25$ (gray), $H = 0.50$ (red), and $H = 0.75$ (cyan), the central 256 by 256 pixel region of the image is analyzed by the power spectrum methodology. The log-log plot of power versus frequency is seen in which the linear region is shown through the colored line above the power spectral signal.

fBm series into two parts, R_n and S_n, for which the ratio of $\frac{R_n}{S_n}$ is calculated [48]. The division of the 1D fBm signal is repeated until the length of each divided signal is 2. The log-log plot of $\frac{R_n}{S_n}$ versus the number of iterations n allows for the calculation of H. Comparing the wavelet transform (WT), power spectral, RL, and R/S methodologies in the calculation of H in 1D fBm signals, Chamoli et al. 2007 found the WT and R/S methods to perform the best in short and long term series [49]. However, the power spectral methodology was tested on both 1D and 2D fBm signals versus a variety of wavelets. The power spectral methodology produced a more consistent calculation of H in fBm images [50]. Validating this conclusion on tomographic brain CT images, Parra et al.

2003 found the extraction of H from the frequency domain to be more reliable [50]. Dlask et al. 2022 implemented the maximum likelihood methodology for the comparison of benign versus cancerous lumps' H in mammograms [51].

CHAPTER 5

IMPROVING THE 2D WTMM METHODOLOGY AND POWER SPECTRAL ANALYSIS

5.1 2D WTMM Parameter Tuning

5.1.1 Current Autofit Methodology

The current 2D WTMM methodology for analyzing the tissue microenvironment of grayscale mammograms begins with the sliding window analysis [9, 10]. A sliding window of 360 by 360 pixels iterate over the mammograms with a 32-pixel step size creating thousands of overlapping mammographic subregions. Each subregion is then fed to the 2D WTMM methodology in which the central 256 by 256 pixel region of the subregion is analyzed to avoid edge effects (Figure 5.1). The WT (Equation 4.1) is computed on these
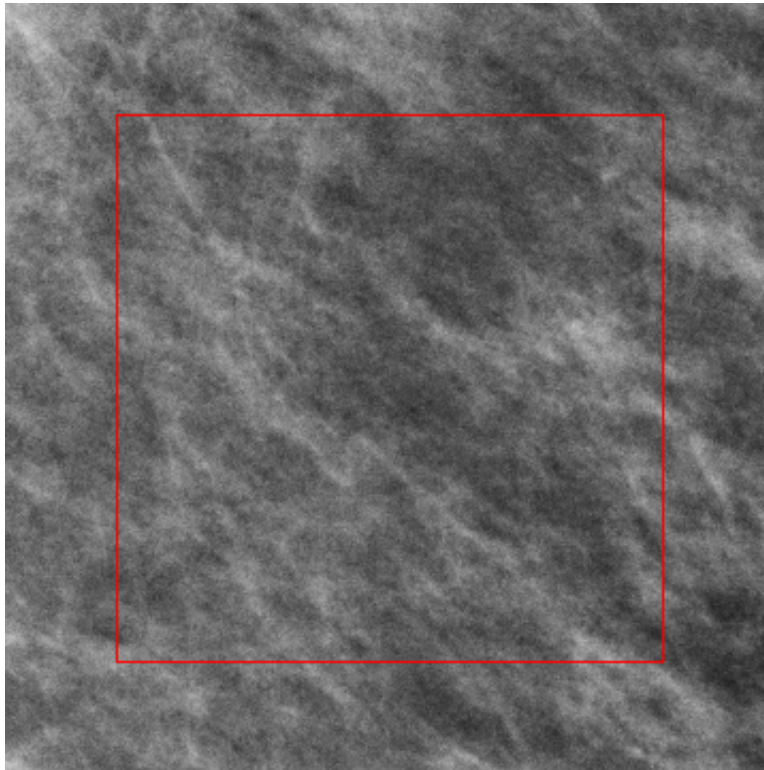
Figure 5.1: A sample mammographic tissue subregion of size 360 by 360 pixels. The red rectangle indicates the central 256 by 256 pixel region kept for analysis to avoid edge effects.

Table 5.1: List of q-values and their associated weights using the 2D WTMM sliding window analysis.

q	-2.0	-1.5	-1	-0.5	-0.3	-0.2	-0.1	0	0.1	0.2	0.3	0.5	1	1.5	2	2.5	3.0
Weight	0.1	0.5	1	3	5	7	9	10	9	8	7	5	3	2	1	0.5	0.2

subregions from wavelet scale $a \sim 7$ pixels to $a \sim 120$ pixels allowing for the WTMM chains to be created for wavelet scales a. With the WTMM chains created, the WTMMM can be acquired allowing for the creation of the WT skeleton $\mathcal{L}(a)$, the calculation of the partition function (Equation 4.7), $h(q, a)$ curves (Equation 4.11), and $D(q, a)$ curves (Equation 4.12) [9, 10, 11, 52, 44, 12, 53]. Once the sliding window mechanism is complete, each subregion can be passed to the multi-fractal analysis. A fitting window is performed on the $D(q, a)$ vs $\log_2(a)$ curves (Figure 5.2b) and $h(q, a)$ vs $\log_2(a)$ curves (Figure 5.2c) to find the most linear portion of these curves to extract a slope. The lower bound a_{min} for this fitting window is varied from $\log_2(a_{min}) = 0.0, 0.1, ...2.1$, as the upper bound a_{max} is also varied from $\log_2(a_{max}) = 1.0, 1.1, ...4.1$ with $MinADelta = a_{max} - a_{min}$. For each (a_{min}, a_{max}) window, the coefficient of determination R^2 is calculated for $h(q = 0)$ and $D(q = 0)$, denoted as $R^2_{h(0)}$. For all q-values (Table 5.1), the weighted standard deviation of H over all q-values and the weighted mean of R^2 over all $h(q, a)$ curves are calculated to evaluate the goodness of fit. These metrics are denoted as sd_w and $<R^2w>$, respectively. Marin et al. 2017 determined that the following conditions must be met for the specific fitting window to be kept [9]:

I. $-0.2 < h(q = 0) < 1.0$

II. $1.7 < D(q = 0) < 2.5$

III. $R^2_{h(0)} > 0.96$

IV. $sd_w < 0.06$

V. $< R^2_w >> 0.96$.
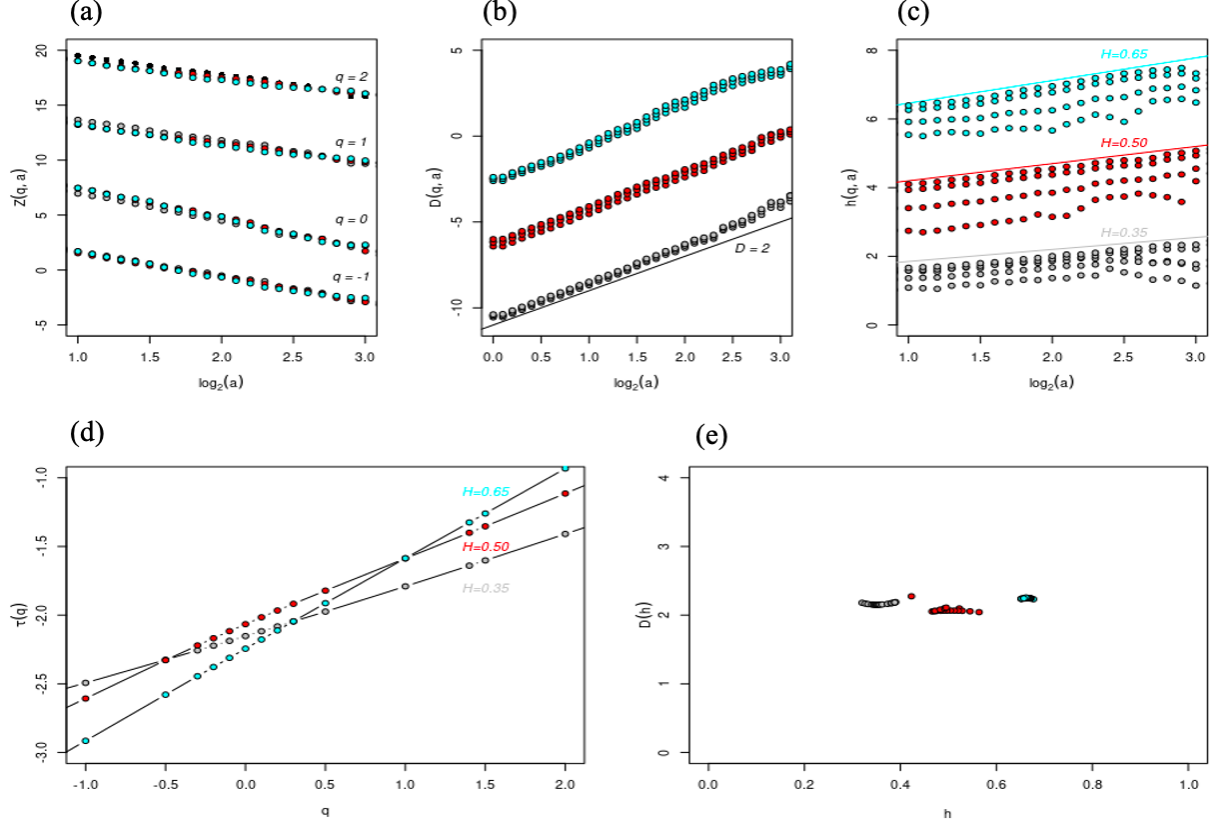
Figure 5.2: Sliding window 2D WTMM analysis with the Gaussian smoothing function for mammographic fatty, risky dense, and healthy dense tissue regions, with estimated $H = 0.35$ (gray), $H = 0.50$ (red), and $H = 0.65$ (cyan), respectively. $Z(q, a)$ (Eq. 4.7), $D(q, a)$ (Eq. 4.12), and $h(q, a)$ (Eq. 4.11) versus $\log_2(a)$ for q-values ranging from -1 to 2 (a-c). $\tau(q)$ (Eq. 4.9) versus q (d). The monofractality of the mammographic subregions are confirmed through the linearity of $\tau(q)$ and clustering of $D(h)$ (Eq. 4.10) (e).

Condition (I) represents the H for an image's singularity spectrum $h(q = 0)$ [9]. The range exists to ensure no regions posses an $H > 1$ as this is the upper limit that can be estimated with first-order wavelets. Condition (II) ensures $D(h) \sim 2$ (Equation 4.10) i.e. the domain is dense. Condition (III) ensures $h(q = 0)$ is sufficiently linear to extract a viable slope from the fitting window. Condition (IV) ensures the surface is monofractal. The threshold checks if the $h(q, a)$ curves are parallel to one another, thus representing a H within a standard deviation of 0.06 across all q values. Finally, condition (V) analyzes the linearity of all $h(q, a)$ curves, while giving more weight to the curves closer to $h(q = 0)$. If a subregion passes these conditions, H can be obtained by calculating the slope of $h(q = 0)$

within the $(\log_2(a_{min}), \log_2(a_{max}))$ fitting window. However, if a subregion does not pass these conditions, it is rejected from the 2D WTMM sliding window analysis and classified as a no-scaling region. The resulting H from the autofit analysis classifies the mammographic subregions into three categories: $H \leq 0.45$ (gray), $0.45 < H < 0.55$ (red), and $H \geq 0.55$ (cyan) (Figure 5.3). Respectively, these categories are a description of anti-correlated fluctuations (fatty tissue), uncorrelated density fluctuations (risky dense tissue), and correlated density fluctuations (healthy dense tissue) [9].

5.1.2 Implementation of the Mexican Hat Wavelet

In order to investigate the efficiency of the current autofit methodology, a goal of this thesis was to implement the Mexican hat rather than the Gaussian smoothing function employed in the current state of the 2D WTMM sliding window analysis [9, 10]. The Mexican hat is simply the second derivative of the Gaussian smoothing function. The visual and mathematical differences can be seen in Figure 4.1 and Equation 4.2, respectively. The higher wavelet order of the Mexican hat smoothing function $n_\psi = 3$ can be directly related to the increased amount of vanishing moments, which in the multi-scale context of the 2D WTMM methodology, has been shown to increase scaling efficiency [11, 44]. A more populated $\mathcal{L}(a)$ (Figure 4.3) is likely due to the higher order nature of the Mexican hat smoothing function.

5.1.3 Calibration analysis on fBms

A total of 500 fBm calibration images per $H \in [0.00, 1.00]$ were analyzed through the use of the Mexican hat to evaluate its performance in comparison with the Gaussian smoothing function in the 2D WTMM methodology. The mean and standard deviation of the calculated H from both the Gaussian and Mexican hat smoothing functions from 0.00 to 1.00 in 0.05 increments as shown in Figure 5.4. These initial results demonstrate the Mexican hat outputs an experimental mean H closer to the theoretical H (H_{theo}) in comparison with the Gaussian smoothing function.
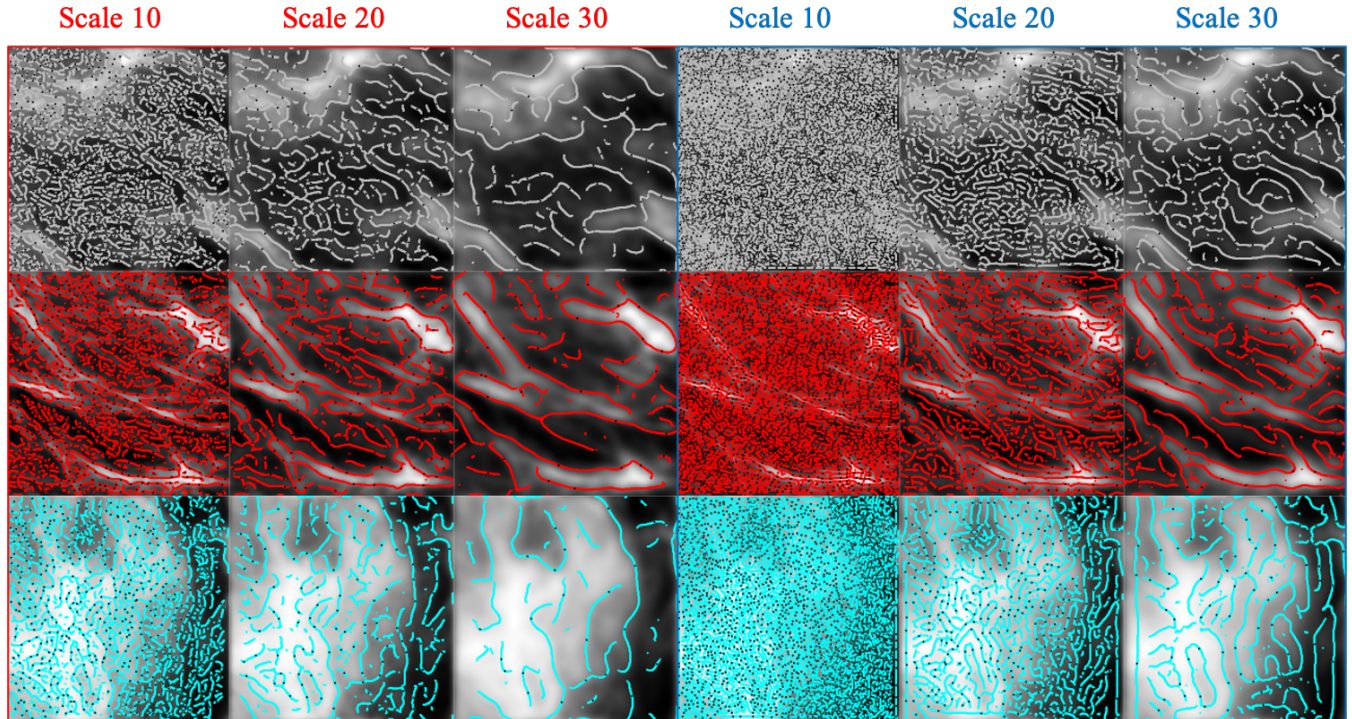
Figure 5.3: WTMM chains are shown for the Gaussian (shown in red text) and Mexican hat (shown in blue text) smoothing functions at wavelet scales $a = 2^1\sigma_w$, $2^2\sigma_w$, and $2^3\sigma_w$ (where $\sigma_w = 7$ pixels). Throughout all wavelet scales a, the higher wavelet order nature of the Mexican hat causes for more WTMM chains to be produced across all wavelet scales a in comparison with the Gaussian.

5.1.4 Changing the R^2 Threshold

The coefficient of determination R^2 defined as

$$
\begin{aligned}
R^2 &= 1 - \frac{\text{sum squared regression (SSR)}}{\text{total sum of squares (SST)}} \\
&= 1 - \frac{\sum(y_i - \hat{y})^2}{\sum(y_i - \bar{y})^2}
\end{aligned}
\tag{5.1}
$$

is used to evaluate the goodness of fit along the $h(q, a)$ curves (Figure 5.2c). For experimental H values close to 0, $\bar{y}$ is similar to the expected value, causing the value of R^2 to equal -Infinity, which make condition (III) fail. Thus, the standard deviation for the experimentally calculated $H \in [0.00, 0.10]$ is quite high (Figure 5.4). Varying the R^2 threshold from 0.80 to 0.95 in 0.05 and from 0.95 to 0.99 in 0.01 increments, respectively, demonstrates a higher amount of no-scalings across $H \in [0.00, 0.10]$ until $R^2 = 0.95$. For $R^2 > 0.95$, no-scaling values begin to be seen for $H > 0.10$. The amount of no-scalings for the Mexican hat is consistently less than the Gaussian smoothing function (Figure 5.5).
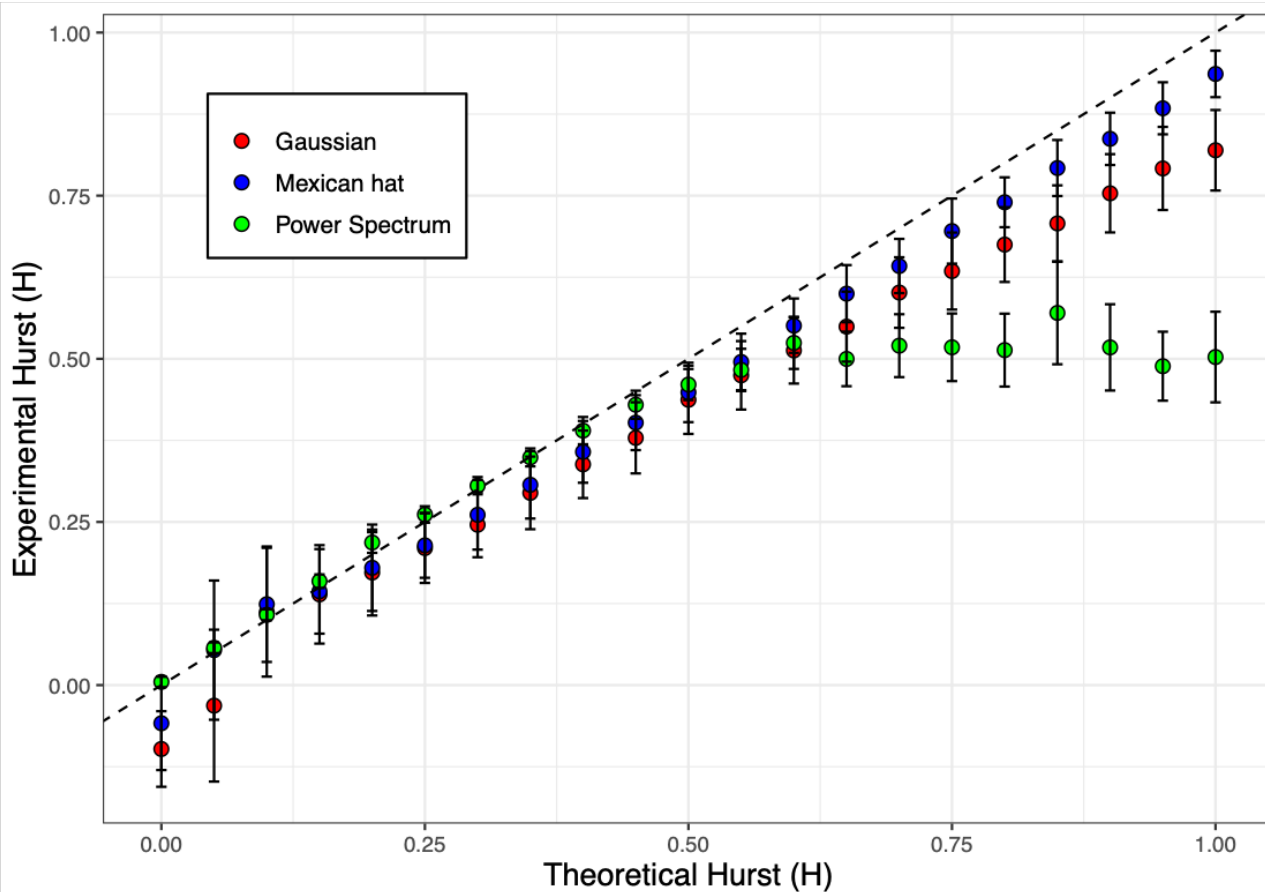
Figure 5.4: The power spectrum and 2D WTMM methodologies were used to analyze 500 fBm calibration images across $H_{theo} \in [0.00, 1.00]$ in 0.05 increments for both the Gaussian and Mexican hat smoothing functions. The mean and standard deviation of calculated H through the Gaussian (red), Mexican hat (blue), and power spectrum (green) methodologies is plotted against H_{theo}. $H_{theo} = H_{experimental}$ is shown through the dotted black line.

5.1.5   Changing the Minimum Value of H

For $H_{theo} \in [0.00, 0.10]$, a high amount of no-scalings is seen when calibrating the Gaussian and Mexican hat smoothing functions on fBm images. The minimum value of H $MinH$ allowed from the autofit analysis is -0.2; however, this was changed to 0.0 to examine the amount of no-scalings for $H \in [0.00, 0.10]$ (Figure 5.6). An even higher amount of no-scaling values can be seen when $MinH = 0.0$ for both the Gaussian and Mexican hat smoothing functions. Regardless of the increased amount of no-scalings, the effect of changing $MinH$ can be evaluated through the use of Root-Mean Square Error (RMSE) defined as
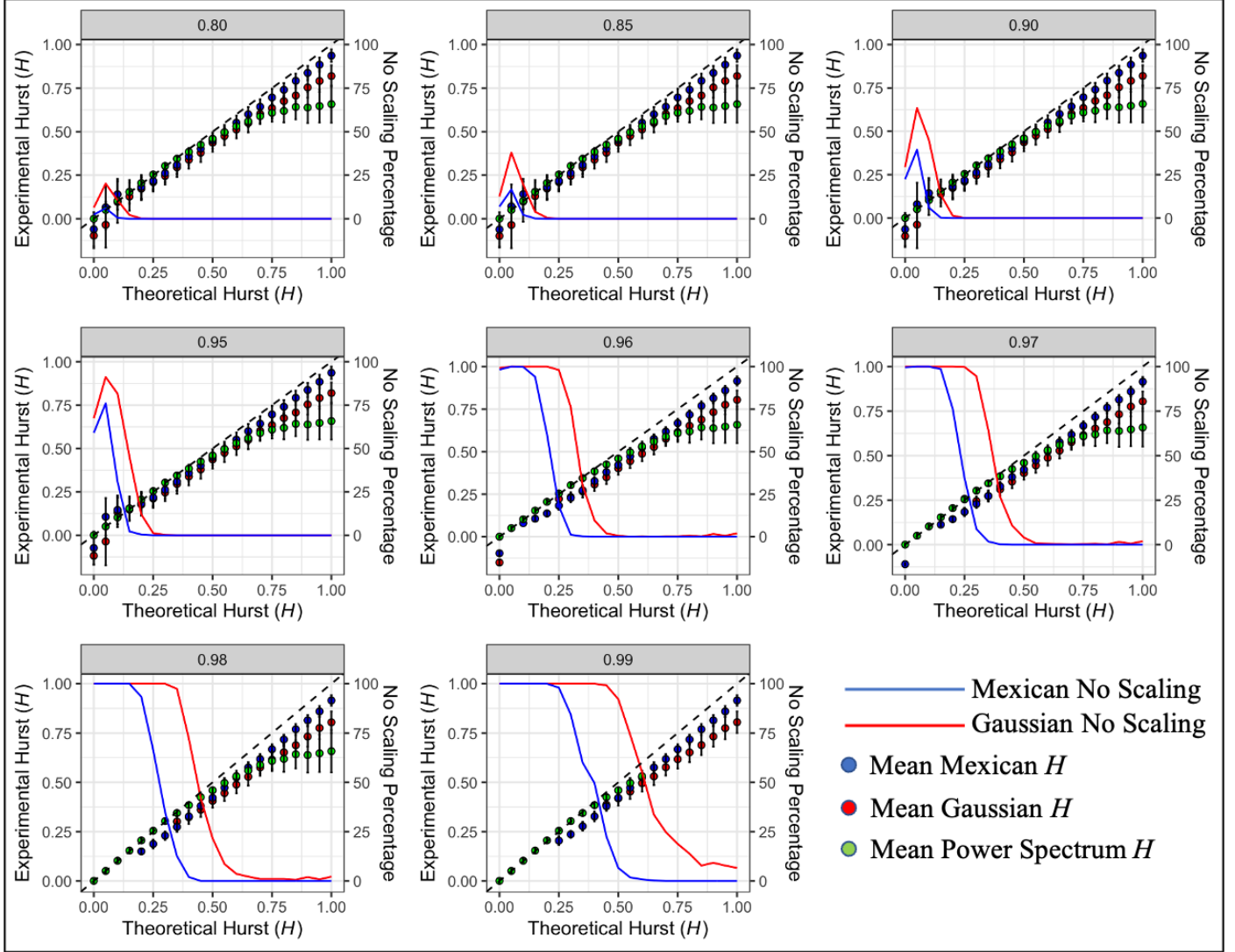
Figure 5.5: The R^2 threshold is varied from 0.80 to 0.99 in the 2D WTMM and power spectrum methodologies. The mean, standard deviation, and no-scaling counts are shown for the Gaussian (red) and Mexican hat (blue) smoothing functions, and the power spectrum methodology (green).

$$RMSE = \sqrt{\left(\frac{1}{N}\right) \sum_{i=1}^{n} (\hat{y}_i - y_i)^2} \tag{5.2}$$

where N is the number of simulated fBm images, $\hat{y}_i$ is H_{theo}, and y_i is the experimental calculation of H. Considering both $H \in [0.00, 0.45[$ and $H \in [0.00, 1.00]$, RMSE indicates changing $MinH$ to 0.0 does not yield a more efficient calculation of H (Table 5.2).

27
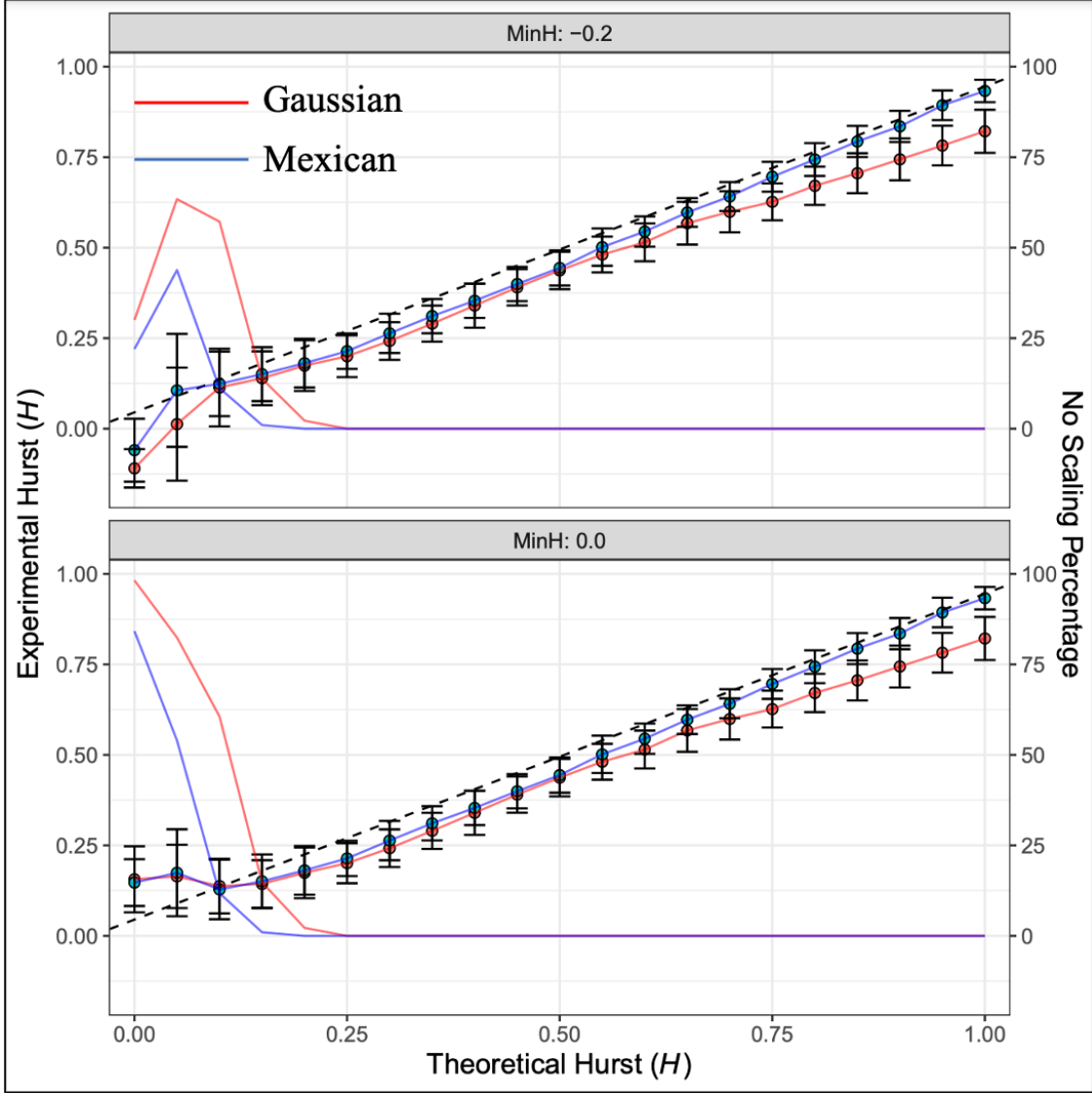
Figure 5.6: The minimum value of H, $MinH$, allowed from the 2D WTMM sliding window analysis is changed from -0.2 to 0.0 to examine the effect on H calculation. fBm images rejected from the analysis, also known as no-scalings, due to not meeting the required conditions are shown through the line plot for both Gaussian (red) and Mexican hat (blue) smoothing functions.

5.1.6 Changing the Distance Between a_{min} and a_{max}

The current 2D WTMM sliding window analysis employs an iterative loop over wavelet scales a for an image's $h(q, a)$ and $D(q, a)$ curves (*Section 5.1.1*). H is calculated from the slope of the most linear region of $h(q = 0)$ [9, 10]. In order to address the amount of no-scalings in the current version of the 2D WTMM analysis, especially for $H \in [0.00, 0.10]$, this iterative loop across the wavelet scales a for an image's $h(q, a)$ curves

is revisited (Figure 5.7). In its default and initial implementation, the lower $\log_2(a_{min})$ and upper $\log_2(a_{max})$ bound of the window is varied by a factor of 0.1. The distance between $\log_2(a_{min})$ and $\log_2(a_{max})$, denoted as $MinADelta$, is 1.0. $MinADelta$ is varied from 1 to 5 in 0.5 increments and RMSE is used to evaluate how this change affects the accuracy of the calculated H (Figure 5.8 and Table 5.3) [9, 10].
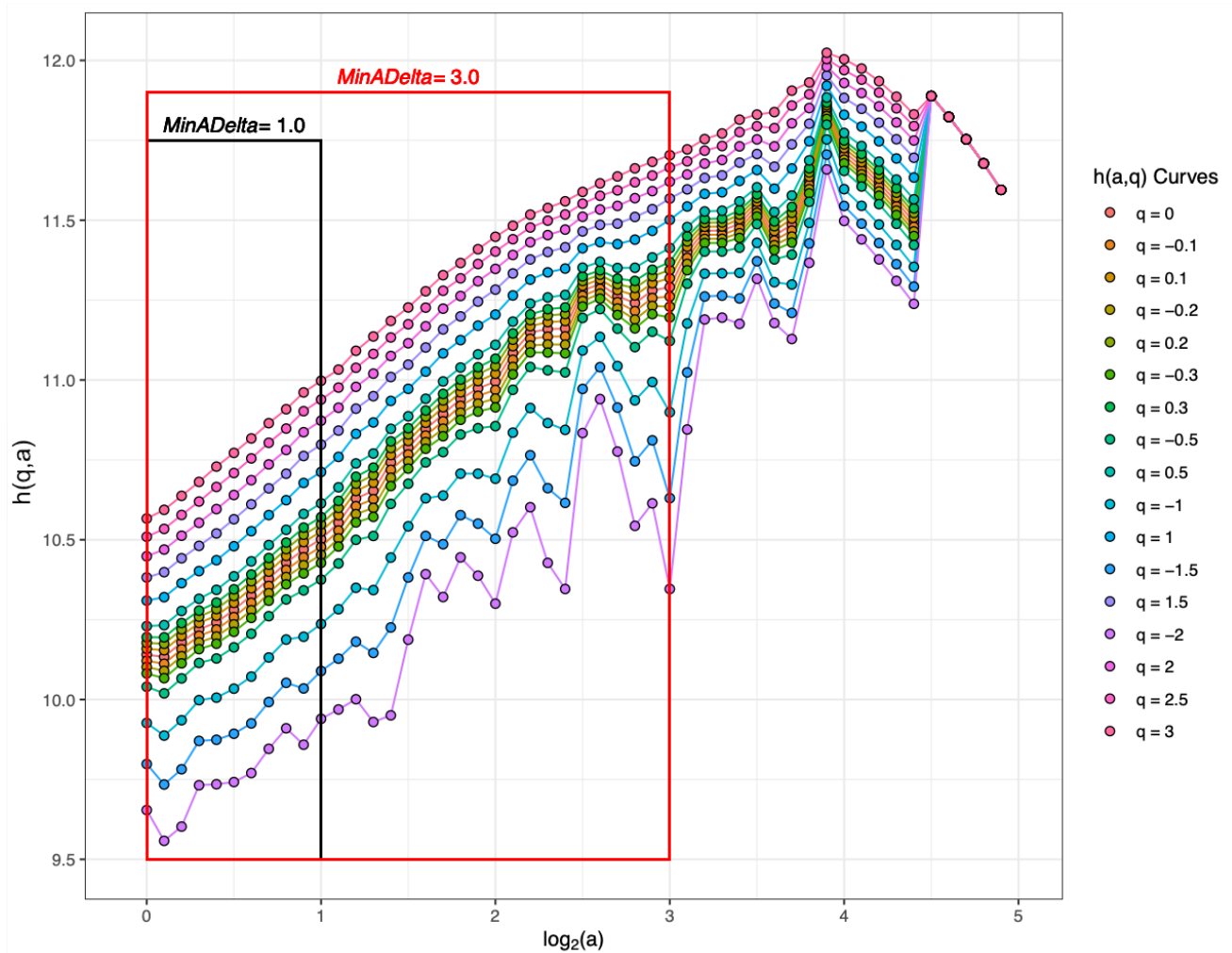
Figure 5.7: Demonstration of the sliding window's minimum size, $MinADelta$, across the $h(q, a)$ curves for an fBm image ($H = 0.5$).

5.2 Improving the Power Spectral Analysis

The power spectrum is efficient in calculating H from fBm images for which $H_{theo} < 0.50$ (Figure 5.9). In order to examine how the power spectrum analysis can be

Table 5.2: RMSE is used to evaluate the performance of the 2D WTMM, with both the Gaussian and Mexican hat smoothing functions, and power spectrum methodologies in fBm images. The power spectrum has the lowest RMSE for $H \in [0.00, 0.45[$ while the Mexican hat demonstrates the lowest RMSE for $H \in [0.45, 1.00]$.

	$H \in [0.00, 0.45[$			$H \in [0.45, 1.00]$			$H \in [0.00, 1.00]$		
R2 Threshold	Gaussian	Mexican	Power Spectrum	Gaussian	Mexican	Power Spectrum	Gaussian	Mexican	Power Spectrum
0.80	0.05827	0.03754	0.01002	0.12703	0.05757	0.20027	0.09743	0.04869	0.13865
0.85	0.05867	0.03807	0.01002	0.12703	0.05757	0.20027	0.09754	0.04889	0.13865
0.90	0.06010	0.03950	0.01002	0.12703	0.05757	0.20027	0.09795	0.04943	0.13865
0.95	0.06251	0.04392	0.01002	0.12703	0.05757	0.20027	0.09867	0.05117	0.13865
0.96	0.09457	0.06796	0.01002	0.14737	0.08166	0.20027	0.12843	0.07564	0.13865
0.97	0.07209	0.07247	0.01002	0.14733	0.08166	0.20027	0.12565	0.07776	0.13865
0.98	0.07334	0.06742	0.01002	0.14720	0.08166	0.20027	0.13137	0.07675	0.13865
0.99	0.06280	0.06597	0.01002	0.14566	0.08169	NaN	0.13623	0.07696	0.27968

improved to provide more accurate calculations of H, varying the R^2 threshold, the fBm image size, and the optimal spatial frequency range was explored.

5.2.1 Changing the R^2 Threshold

One characteristic needed to acquire the linear portion of the power spectral signal is a suitable R^2 threshold. The R^2 threshold was varied from 0.80 to 0.95 in 0.05 increments and from 0.95 to 0.99 in 0.01 increments, respectively. A lower standard deviation across H values acquired from the power spectrum methodology is seen as R^2 is increased until $R^2 = 0.99$ (Figure 5.5). At this point, mean and standard deviation of H are not able to be calculated due to the lack of fBm log transformed power spectral signals that have a linear portion with an $R^2 \geq 0.99$.

5.2.2 Changing Image Size

As discussed previously, the current sliding window methodology involves the creation of 360 by 360 pixel subregions for analysis in the 2D WTMM and power spectrum methodology. To examine how this methodology can be improved, various fBm image sizes and power spectral signal lengths are created and tested with the power spectrum methodology. Through increasing fBm image size and the length of the log transformed power spectral signal, the experimental mean of calculated H decreases for $H_{theo} \geq 0.65$, while the standard deviation increases (Figure 5.9).
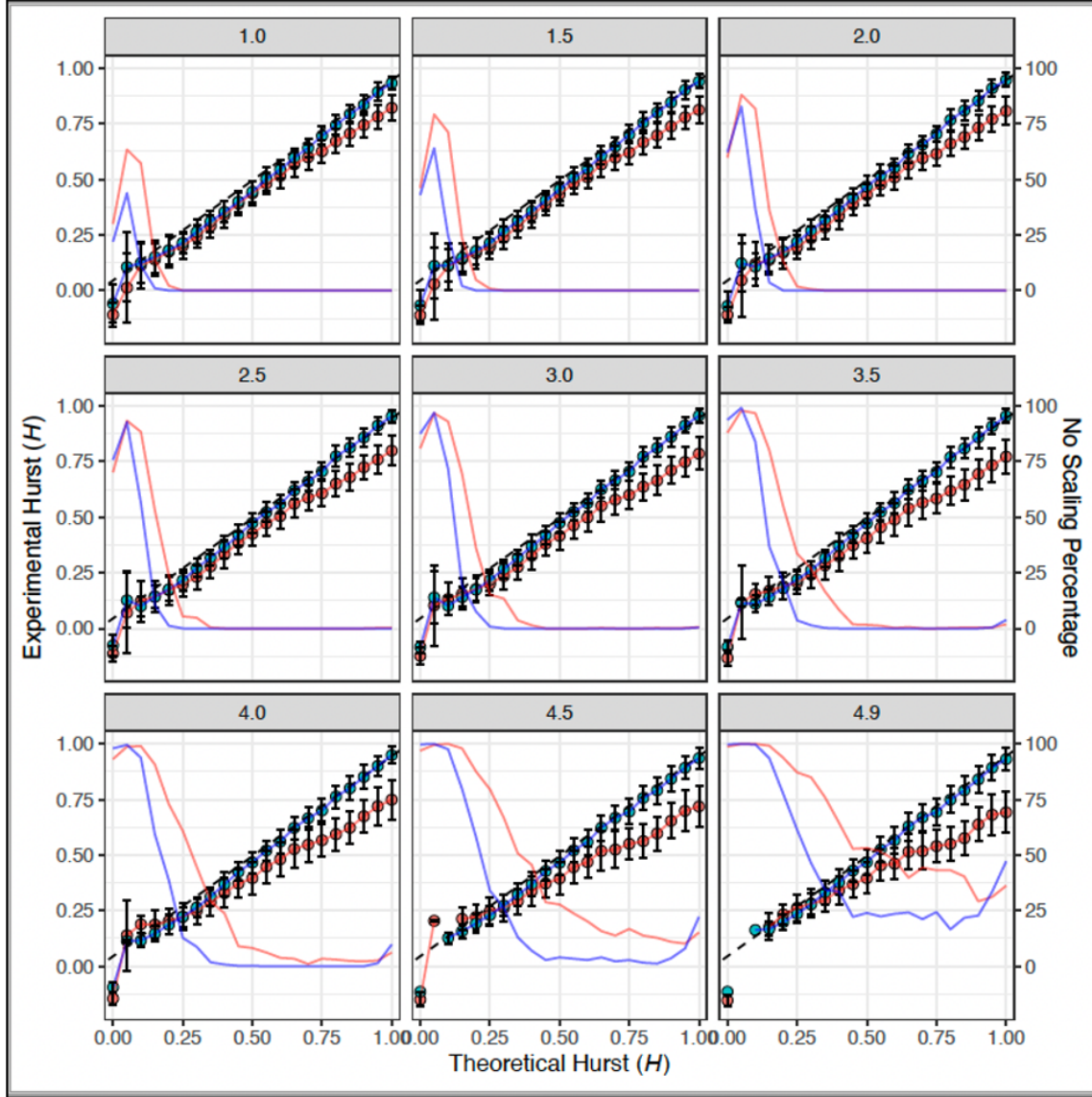
Figure 5.8: To calculate H in the 2D WTMM sliding window analysis, the $h(q = 0)$ curve is analyzed through a sliding window analysis of size $MinADelta$. $MinADelta$ is varied from 1.0 to 4.9 in which the mean, standard deviation, and no-scaling counts are shown for the Gaussian (red) and Mexican hat (blue) smoothing functions.

5.2.3   Calibrating Spatial Frequency Range along a Power Spectral Signal

The power spectrum methodology, regardless of the threshold changes, is able to accurately classify H experimentally in fBm images for $H_{theo} < 0.45$. If mammographic power spectral signals are found to be similar to the fBm power spectral signals, fBm calibration demonstrates the power spectrum methodology can be applied to classify fatty tissue in mammograms in a much faster manner than the 2D WTMM methodology.

Table 5.3: RMSE is used to evaluate the performance of the 2D WTMM methodology with both the Gaussian and Mexican hat smoothing functions in fBm images. The Mexican hat demonstrates a lower RMSE than the Gaussian smoothing function regardless of $MinADelta$.

MinADelta	$H \in [0.45, 1.00]$		$H \in [0.00, 1.00]$	
	Gaussian	Mexican	Gaussian	Mexican
1.0	0.13582	0.07137	0.11801	0.07668
1.5	0.13990	0.06594	0.12070	0.06881
2.0	0.14491	0.05900	0.12480	0.06077
2.5	0.15308	0.05495	0.13208	0.05602
3.0	0.16521	0.05357	0.14314	0.05392
3.5	0.18078	0.05685	0.15809	0.05538
4.0	0.19884	0.06381	0.17678	0.06022
4.5	0.22014	0.07243	0.19953	0.06706
4.9	0.23481	0.07546	0.21541	0.06986

Table 5.4: RMSE is used to evaluate the power spectrum methodology's calculation of H for fBm image sizes of 360, 512, and 1024 with signal lengths of 128 and 256 points for $H \in [0.00, 0.45[$ and $H \in [0.00, 1.00]$

fBm Image Size	Number of Points	$H \in [0.00, 0.45[$	$H \in [0.00, 1.00]$
360	128	0.01480	0.07152
	256	0.00500	0.11147
512	128	0.00555	0.07958
	256	0.00526	0.11449
1024	128	0.00775	0.11807
	256	0.00554	0.13369

However, an issue in calculating H from the log transformed power spectral signal is the acquisition of the spatial frequency range defined with lower k_{min} and upper k_{max} bounds. Since the power spectrum methodology is being applied to fatty tissue regions, a R^2 threshold of 0.99 can be used to ensure for the most accurate linear region of the power spectral to be extracted. The spatial frequency range is fixed by taking the median of k_{min} and k_{max} output through applying the power spectrum methodology to all 500 fBm calibration images for each $H \in [0.00, 1.00]$. Thus, for each mammographic subregion H is calculated by the slope of the power spectrum signal in

$[\log_2(k_{min}), \log_2(k_{max})] = (2.096, 7.096)$.
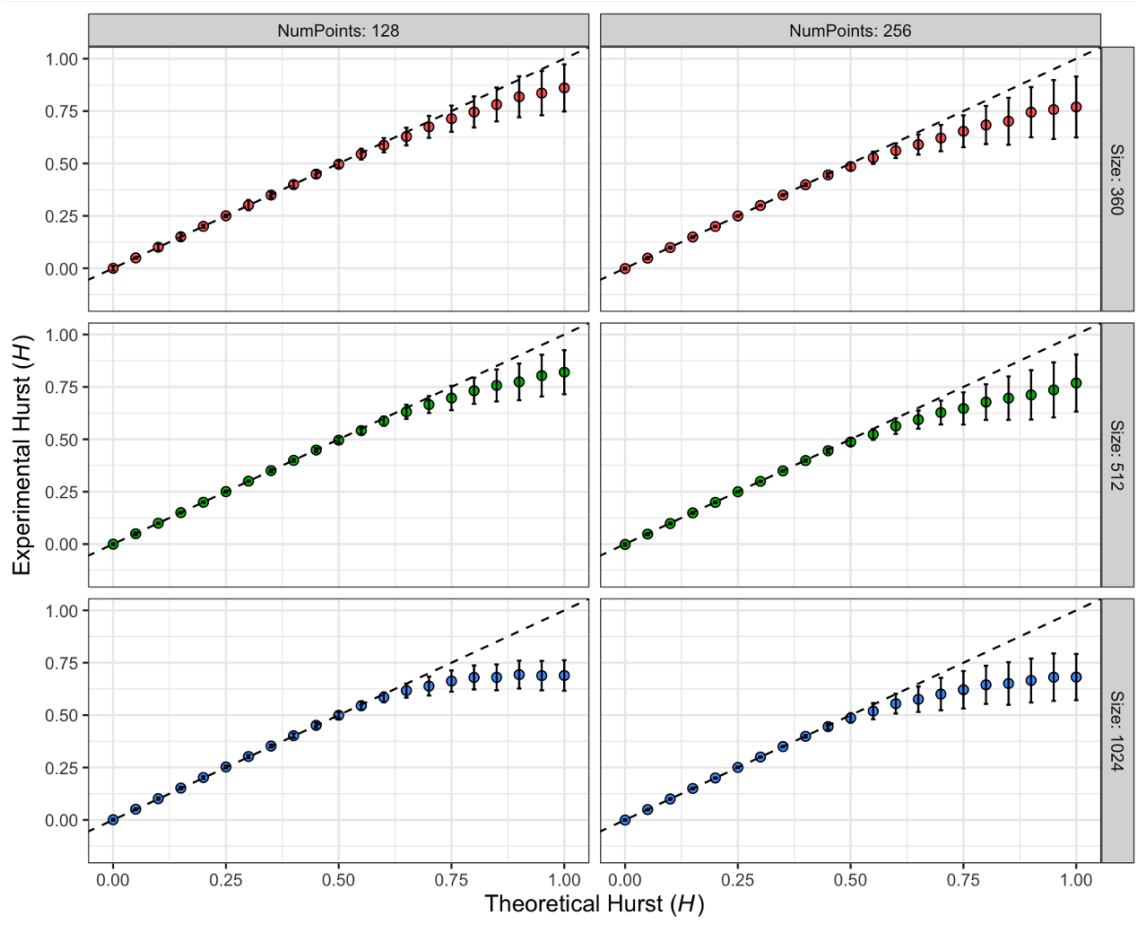
Figure 5.9: Power spectrum method results on fBm images with size 360, 512, and 1024 are seen for power spectral signal lengths of 128 and 256 points.

5.3   Calibration Results

RMSE was used to evaluate the efficiency of the 2D WTMM, with the Gaussian and Mexican hat smoothing functions, and the power spectral methodologies in the calculation of H in fBM images. Through varying $MinADelta$, the Mexican hat consistently demonstrates a lower RMSE (Table 5.3). As we increase $MinADelta$, an increased amount of no-scalings are seen for both the Gaussian and Mexican hat smoothing functions (Figure 5.8). Increasing the R^2 threshold in the 2D WTMM methodology increases the amount of no-scalings and RMSE values for both the Gaussian and Mexican hat smoothing functions (Table 5.2 and Figure 5.5). For fBM images with $H_{theo} \in [0.00, 0.45[$, the power spectral analysis demonstrates the lowest RMSE values, thus highlighting its efficiency in

calculating H in fBm images with a known anti-correlated H. However, for fBm images with $H_{theo} \in [0.00, 1.00]$, the Mexican hat smoothing function has the lowest RMSE, while the power spectral methodology has the highest RMSE (Table 5.2 and Figure 5.5). Altering fBm image size and power spectral signal size increases the RMSE of the power spectral analysis for $H_{theo} \in [0.00, 1.00]$, while for $H_{theo} \in [0.00, 0.45[$ the RMSE is decreased (Table 5.4). While the RMSE is decreased, the computational time of the power spectral analysis on these larger images is increased.

CHAPTER 6

MAMMOGRAPHIC IMPLEMENTATION

Two mammographic datasets, previously acquired by the CompuMAINE Laboratory, are used for testing the power spectral and 2D WTMM methodologies. These being the Perm and Maine mammographic datasets. The Perm dataset consists of cancerous and benign subsets with 80 and 22 patients, respectively. The cancerous subset consists of 37 cases of invasive ductal carcinoma (IDC) and 43 cases of invasive lobular carcinoma (ILC), while the benign subset consists of 12 cases of fibroadenoma (fib$_a$) and 10 cases of fibrocystic mastopathy (fib$_m$) [10]. The Maine mammographic dataset consists of cancerous and control subsets of 46 and 27 patients, respectively (Table 6.1).

Table 6.1: Perm and Maine mammographic datasets

Mammographic Dataset	Group	Pathology	Number of Patients
Perm	Benign	Fibroadenoma (fib_a)	12
		Fibrocystic Mastopathy (fib_m)	10
	Cancer	Invasive Ductal Carcinoma (IDC)	37
		Invasive Lobular Carcinoma (ILC)	43
Maine	Cancer	-	46
	Control	-	27

6.1   Power Spectral Results

The power spectral methodology was applied to our initial patient dataset using the median k_{min} and k_{max} values from fBm image calibration (Section 5.2.3). A power spectral signal is acquired from a mammographic subregion and the slope is extracted between the median k_{min} and k_{max} values. When the output power spectral signal from these subregions are fit in this spatial frequency range, the mammographic subregion is always classified as fatty tissue. The innate noise while a patient is receiving a mammogram is responsible for this phenomenon. The power spectral signal from a fBm image is quite linear due to the homogenous nature of the image. A mammographic power spectral signal does not fully

share this degree of linearity indicating the median k_{min} and k_{max} values should be re-calibrated on fBm images induced with various degrees of white noise (Figure 6.1).
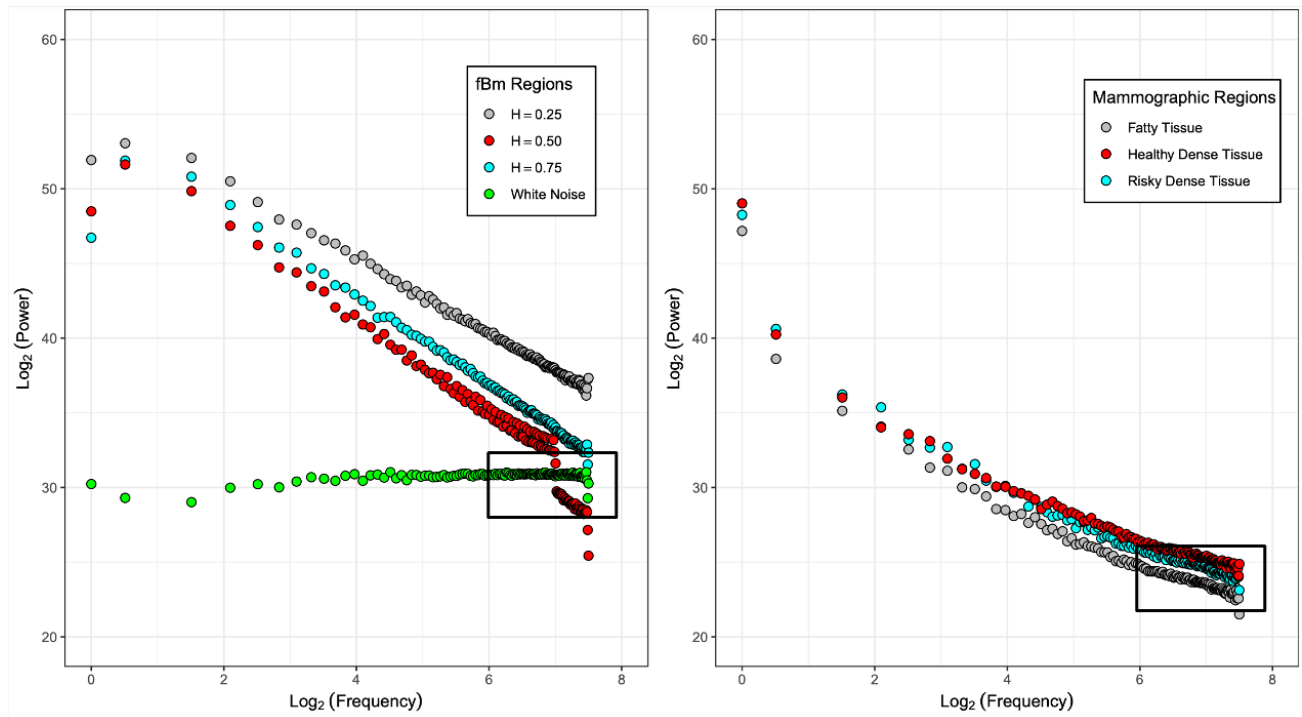
Figure 6.1: Power spectral signals for fBm images with $H = 0.25$ (gray), $H = 0.50$ (red), and $H = 0.75$ (cyan) are plotted with a power spectral signal of a 360 by 360 pixel white noise image (green) (left). Three power spectral signals are plotted for fatty (gray), risky dense (red), and healthy dense (cyan) mammographic tissue regions (right). The black box indicates the similarity of the mammographic and white noise power spectral signals at high frequencies.

The power spectrum methodology can be applied to a white noise influenced fBm image to mimic the noise seen in a mammographic subregion, as seen through the black box in Figure 6.2. First, a white noise image is created in Xsmurf with the same dimensions of the fBm image. The white noise image is multiplied by the ratio of the minimum pixel value of the white noise and fBm image, respectively. The degree of white noise in this image is altered through multiplying this ratio by a factor ranging from 0 to 1. Finally, this altered white noise image is added to a fBm image from which the white noise influenced power spectral signal can be obtained (Figure 6.2).

All 500 fBm calibration images of $H_{theo} \in [0.00, 1.00]$ are analyzed with the power spectrum methodology for each white noise percentage ranging from 0 to 100% in 5%
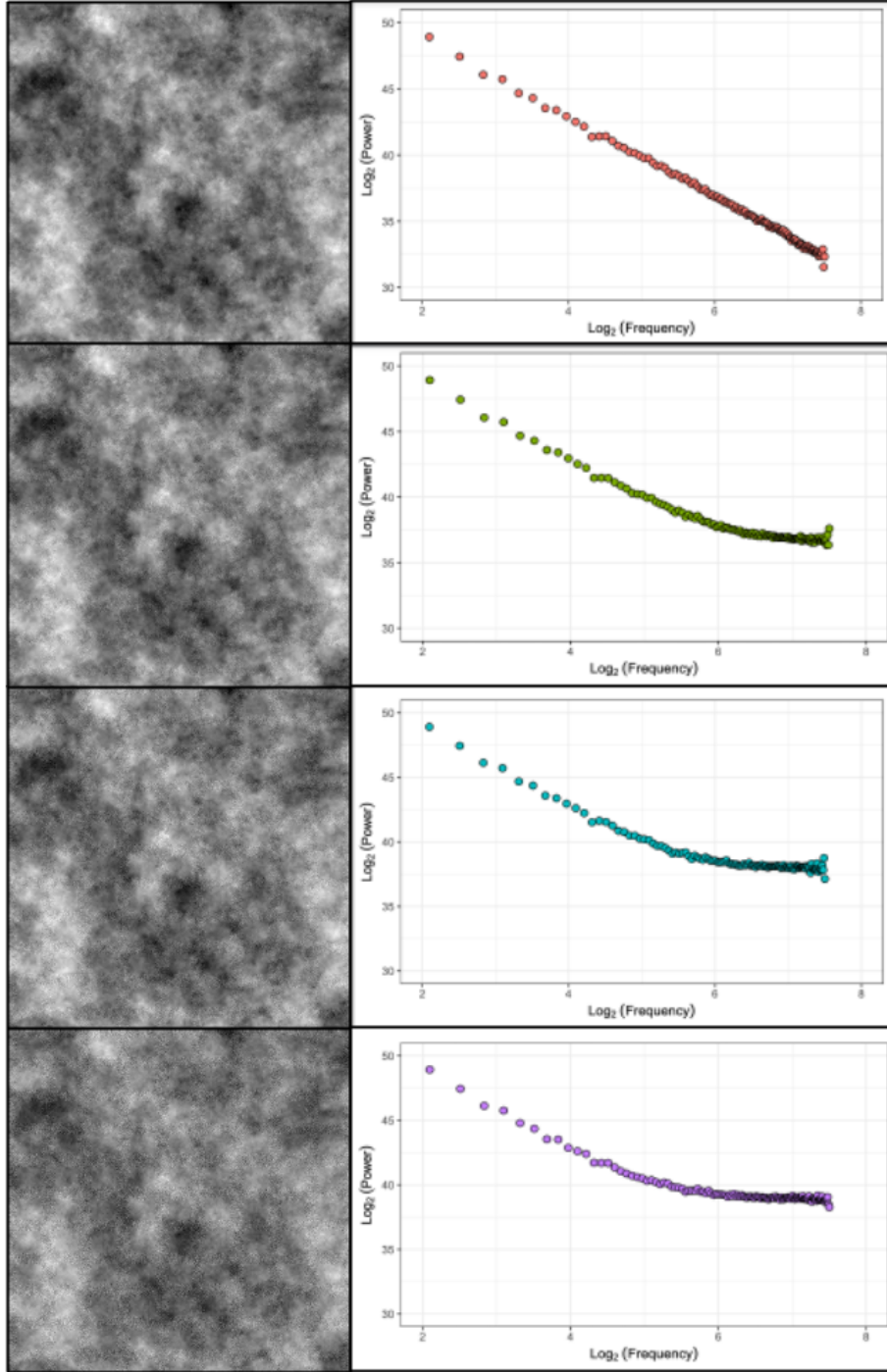
Figure 6.2: fBm images ($H = 0.50$) are influenced with varying levels of white noise. The white noise influenced fBm images of 0% (first row), 25% (second row), 50% (third row), and 75% (fourth row) are plotted alongside their power spectral signal.

increments. The median k_{min} and k_{max} were calculated for each white noise percentage value. We see a decrease in the median k_{max} value as white noise percentage increases

Table 6.2: White noise percentages versus median $\log_2(k_{max})$ calibrated through the power spectrum methodology in fBm images.

Noise %	0.000	0.050	0.100	0.150	0.20	0.250	0.300	0.350	0.400	0.450	0.500	0.550	0.600	0.650	0.700	0.750	0.800	0.850	0.900	0.950	1.000
$log_2(k_{max})$	7.096	5.266	4.904	4.759	4.64	4.599	4.511	4.418	4.319	4.319	4.319	4.319	4.212	4.212	4.096	4.096	4.096	4.096	4.096	4.096	4.096

(Table 6.2). The power spectrum methodology was then applied to all mammograms in the Perm mammographic dataset with each of the white noise fBm calibrated median k_{min} and k_{max}. The initial implementation of the 2D WTMM sliding window analysis with the Gaussian smoothing function utilized the Wilcoxon rank-sum test to demonstrate a statistically significant difference ($p < 0.05$) for fatty, risky dense, and healthy dense breast tissue regions between benign and cancerous mammograms of the Perm dataset [10]. With this, the Wilcoxon rank-sum test was used to evaluate the benign and cancerous mammograms of the Perm dataset with each white noise calibrated k_{min} and k_{max} using the power spectrum methodology. White noise percentages ranging from 0.70 to 1.00 demonstrate a statistically significant difference ($p < 0.05$) in fatty and risky dense breast tissue between benign and cancerous mammograms in the Perm dataset (Table 6.3).

Table 6.3: Median $\log_2(k_{min})$ and $\log_2(k_{max})$ values for each white noise percentage tested on the Perm mammographic dataset using the power spectrum methodology. The p-values seen here are output through the Wilcoxon rank-sum statistical test for the comparison of benign and cancerous mammograms.

Noise %	Fatty Tissue	Risky Dense Tissue	Healthy Dense Tissue	Risky Dense/Fatty Tissue
0.00	NA	NA	NA	NA
0.05	0.8527	0.8462	0.6740	0.8462
0.10	0.9770	0.8660	0.5859	0.8660
0.15	0.7577	0.5291	0.9628	0.5399
0.20	0.4466	0.3057	0.8461	0.3175
0.25	0.4466	0.3057	0.8461	0.3175
0.30	0.3175	0.1867	0.7639	0.1922
0.35	0.1733	0.1249	0.3633	0.1311
0.40	0.1733	0.1249	0.3633	0.1311
0.45	0.1733	0.1249	0.3633	0.1311
0.50	0.1733	0.1249	0.3633	0.1311
0.55	0.1733	0.1249	0.3633	0.1311
0.60	0.1332	0.1024	0.3337	0.1095
0.65	0.1332	0.1024	0.3337	0.1095
0.70	0.0434	0.0409	0.0957	0.0443
0.75	0.0434	0.0409	0.0957	0.0443
0.80	0.0434	0.0409	0.0957	0.0443
0.85	0.0434	0.0409	0.0957	0.0443
0.90	0.0434	0.0409	0.0957	0.0443
0.95	0.0434	0.0409	0.0957	0.0443
1.00	0.0434	0.0409	0.0957	0.0443

6.2 2D WTMM Methodology Results

The implementation of the Mexican hat smoothing function in the 2D WTMM methodology for the calculation of H in fBm images was shown to be more effective than the Gaussian smoothing function (Figure 5.4 and Table 5.2, 5.3). On fBm images, the implementation of a $MinADelta = 3.0$ and the Mexican hat smoothing function produced the lowest value of RMSE (Table 5.3). In order to evaluate if the Mexican hat smoothing function should be incorporated into the 2D WTMM sliding window analysis, the varying of $MinADelta$ is tested for the Gaussian and Mexican hat smoothing functions on the Perm and Maine mammographic datasets. A statistically significant difference in benign versus cancer mammograms is seen in fatty ($p = 0.051$) and risky dense ($p = 0.0005$) tissue of mammograms in the Perm dataset when analyzed with a $MinADelta = 3.0$ and the Mexican hat smoothing function (Figure 6.3). The p-values obtained using these autofit parameters are the lowest seen across all tests using the Gaussian smoothing function (Table 6.4). The increase of $MinADelta$ leads to an increase in no-scalings from both the Gaussian and Mexican hat smoothing functions (Figure 5.8). fBm testing of these parameters demonstrates this is not seen until $MinADelta \geq 4.0$ where we see no-scalings in the Gaussian and Mexican hat smoothing functions for $H_{theo} > 0.45$ (Figure 5.8).

Table 6.4: The 2D WTMM sliding window analysis is tested on the Perm mammographic dataset with the Gaussian and Mexican hat smoothing functions while varying $MinADelta$. The p-values seen here are calculated through the Wilcoxon rank-sum statistical test for the comparison of benign and cancerous mammograms. The greatest significant difference for risky dense breast tissue between benign and cancerous mammograms is seen through the Mexican hat smoothing function with a $MinADelta = 3.0$ in the Perm dataset.

Gaussian			Mexican hat			
Fatty Tissue	Risky Dense Tissue	Healthy Dense Tissue	Fatty Tissue	Risky Dense Tissue	Healthy Dense Tissue	$MinADelta$
0.0125	0.0065	0.0909	0.1512	0.7424	0.0541	1.0
0.0197	0.0078	0.0909	0.0454	0.2964	0.0164	1.5
0.0277	0.0078	0.1311	0.0098	0.0703	0.0133	2.0
0.0601	0.0125	0.2377	0.0055	0.0061	0.0403	2.5
0.0925	0.0250	0.3765	0.0051	0.0005	0.0799	3.0
0.1928	0.0813	0.5353	0.0105	0.0012	0.2135	3.5
0.2631	0.0653	0.9172	0.0472	0.0098	0.4742	4.0
0.5575	0.3241	0.6147	0.0993	0.0593	0.7840	4.5
0.7868	0.6412	0.9934	0.9491	0.4218	0.3992	4.9

Table 6.5: The 2D WTMM sliding window analysis is tested on the Maine mammographic dataset with the Gaussian and Mexican hat smoothing functions while varying $MinADelta$. The p-values seen here are calculated through the Wilcoxon rank-sum statistical test for the comparison of benign and cancerous mammograms. The greatest significant difference for risky dense breast tissue between benign and cancerous mammograms is seen through the Mexican hat smoothing function with a $MinADelta = 1.0$ in the Maine dataset.

Gaussian			Mexican Hat			
Fatty Tissue	Risky Dense Tissue	Healthy Dense Tissue	Fatty Tissue	Risky Dense Tissue	Healthy Dense Tissue	$MinADelta$
0.07885	0.00206	0.01137	0.28845	5.00E-05	0.00189	1.0
0.10328	0.00097	0.00418	0.25545	0.00013	0.00326	1.5
0.05796	0.00348	0.00504	0.21839	0.00027	0.00606	2.0
0.02318	0.00770	0.02042	0.16876	0.00012	0.01502	2.5
0.00700	0.01237	0.02943	0.13266	0.00068	0.01731	3.0
0.00234	0.03024	0.02991	0.06780	0.00236	0.03375	3.5
0.00189	0.07146	0.06497	0.04062	0.01143	0.05665	4.0
0.02200	0.13465	0.07216	0.04533	0.04663	0.22061	4.5
0.04909	0.12228	0.10009	0.19409	0.18077	0.29836	4.9

A statistically significant difference in cancerous versus normal mammograms is seen in risky ($p = 0.0046$) and healthy dense tissue ($p = 0.0413$) for cancerous versus normal mammograms in the Maine dataset when analyzed with a $MinADelta = 1.0$ and the Mexican hat smoothing function (Figure 6.4 and Table 6.5). An $h(q, a)$ curve from a sample mammographic subregion in the Maine dataset demonstrates linearity across all q-values for both the Gaussian and Mexican hat smoothing functions, which is not seen in a sample $h(q, a)$ curve from a mammographic subregion in the Perm dataset (Figure 7.1). An elevated median $\log_2(a_{min})$ between the Maine (0.2) and the Perm (0.9) datasets indicates an increased amount of mammographic noise is present in the Perm dataset attributed to the lack of linearity across q-values for the Gaussian and Mexican hat smoothing functions shown (Table 6.6).

Table 6.6: Median a_{min} and a_{max} in the 2D WTMM analysis for both the Gaussian and Mexican hat smoothing functions for the Perm and Maine mammographic datsets.

	Perm Dataset		Maine Dataset	
	Gaussian	Mexican Hat	Gaussian	Mexican Hat
Median A_{min}	0.9	0.9	0.2	1.1
Median A_{max}	2.4	2.2	1.7	2.4
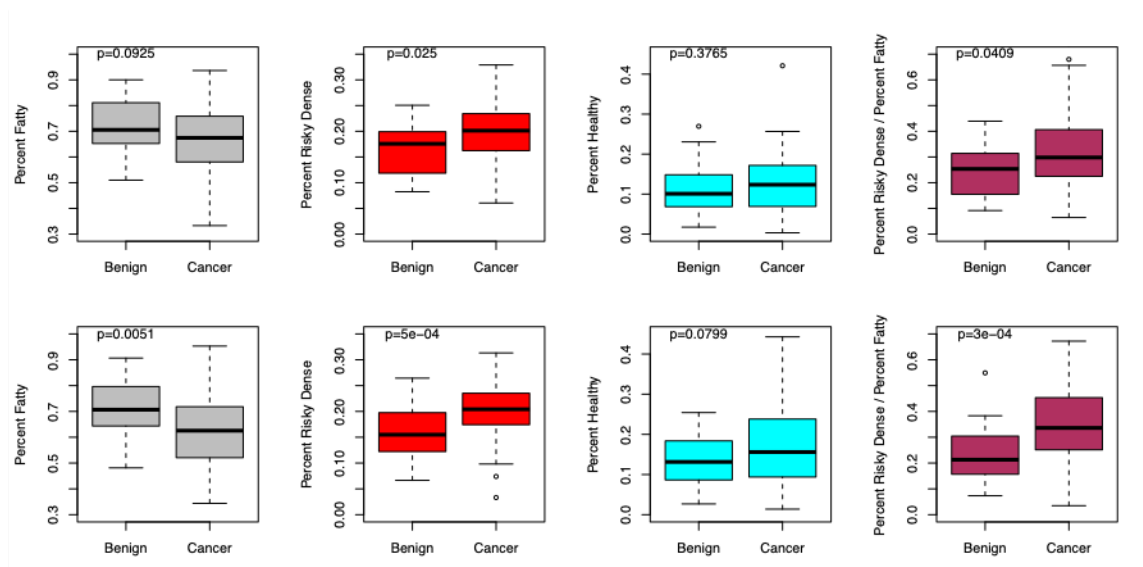
Figure 6.3: The 2D WTMM sliding window analysis analyzed all mammograms in the Perm mammographic dataset with the Gaussian (top row) and Mexican hat (bottom row) smoothing functions. Percent fatty (gray), risky dense (red), healthy dense (cyan), and risky dense over fatty tissue (maroon) are shown for benign and cancerous mammograms. The p-values shown are obtained through the Wilcoxon ranksum statistical test.
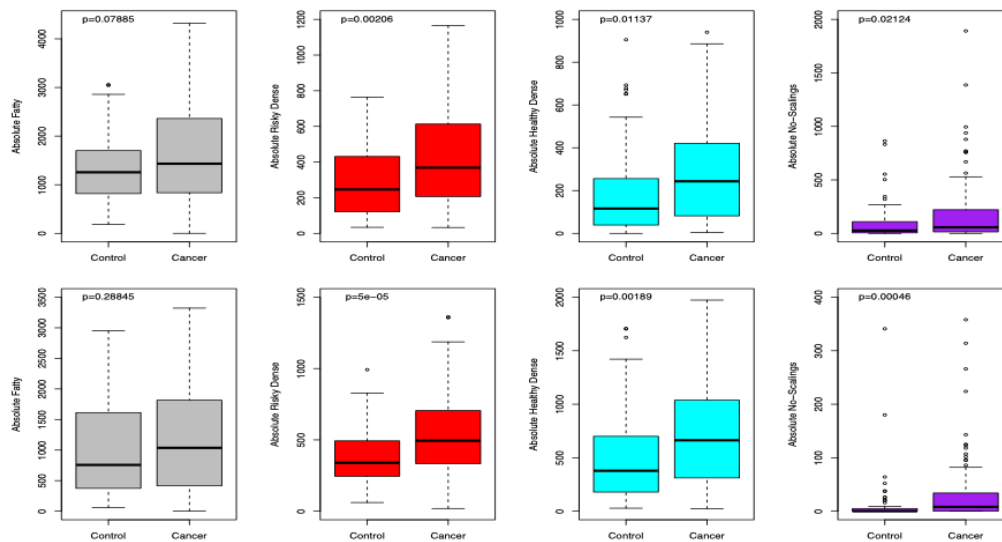
Figure 6.4: The 2D WTMM sliding window analysis analyzed all mammograms in the Maine mammographic dataset with the Gaussian (top row) and Mexican hat (bottom row) smoothing functions. Absolute number of fatty (gray), risky dense (red), healthy dense tissue (cyan) regions, along with the amount of no-scalings (purple), are shown for cancerous and normal mammograms. The p-values shown are obtained through the Wilcoxon ranksum statistical test.

CHAPTER 7

DISCUSSION

7.1 Conclusions

The power spectrum methodology was investigated due to its ease of use and computational efficiency. On fBm images, the power spectrum methodology is more efficient in the calculation of H than the 2D WTMM methodology with the Gaussian and Mexican hat smoothing functions for $H \in [0.00, 0.45[$ (Figure 5.4). The power spectrum methodology's efficiency for $H \in [0.00, 0.45[$ recognition in fBm images inspired the possibility of implementing a combined autofit approach with the 2D WTMM methodology. The power spectrum would be used for $H \in [0.00, 0.45[$ and the Mexican hat smoothing function would be used for $H \in [0.45, 1.00]$. However, the inability of the power spectrum methodology to distinguish fatty from risky and healthy dense tissue renders this combined approach ineffective, regardless of the investigation into white noise calibrated power spectrum signals (Table 6.3).

The 2D WTMM methodology was further examined through replacing the Gaussian smoothing function with its second order derivative, the Mexican hat. The higher order nature of the Mexican hat was hypothesized to provide a more accurate H calculation in fBm and mammographic images. The Mexican hat demonstrates a more accurate H calculation in fBm images than the Gaussian through its associated lower RMSE in comparison with the H_{theo} of the fBm images (Tables 5.2 and 5.3). The implementation of the 2D WTMM sliding window analysis with $MinADelta = 1.0$ demonstrates the Gaussian performs better than the Mexican hat smoothing function in the Perm dataset. However, the implementation of $MinADelta = 1.0$ on the Mexican hat's $h(q, a)$ curves has shown to not be effective on mammograms from the Perm dataset. The high level of noise at small wavelet scales a in the Perm mammographic dataset's $h(q, a)$ curves is attributed to this phenomenon, which is not seen in the mammograms from the Maine patient dataset

(Figure 7.1). The implementation of the Mexican hat with $MinADelta = 3.0$ and $MinADelta = 1.0$, for the Perm and Maine datasets, respectively, demonstrate a greater significant difference in fatty and risky dense breast tissue for benign and cancerous mammograms (Tables 6.4 and 6.5). We are able to conclude the Mexican hat smoothing function should be implemented into the 2D WTMM sliding window analysis to achieve the most efficient recognition of risky dense breast tissue in mammograms, while $MinADelta$ is highly dependent on the quality of mammograms provided.
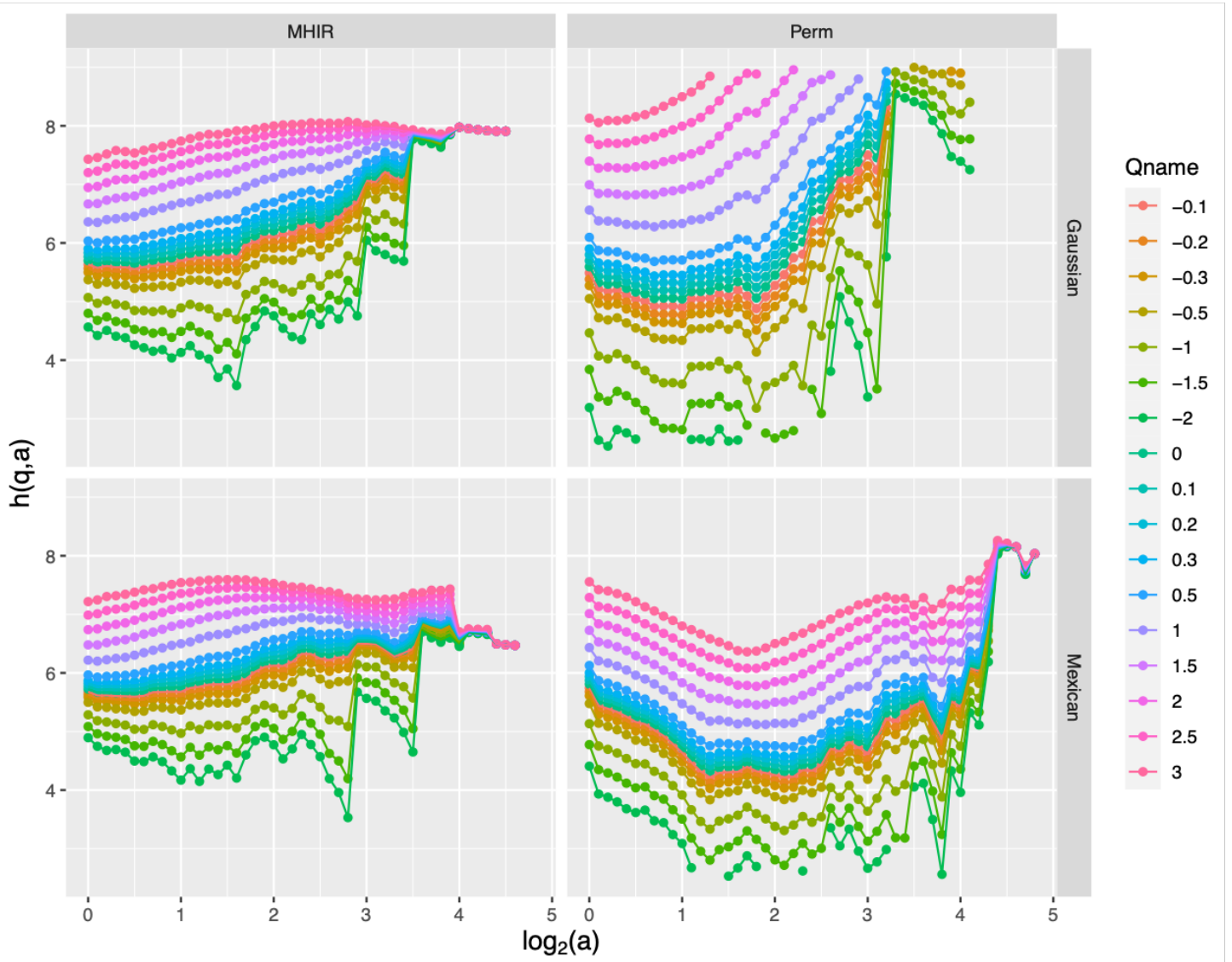
Figure 7.1: $h(q, a)$ curves are seen for both the Gaussian and Mexican hat smoothing functions for a sample mammographic subregion in the Perm and Maine datasets.
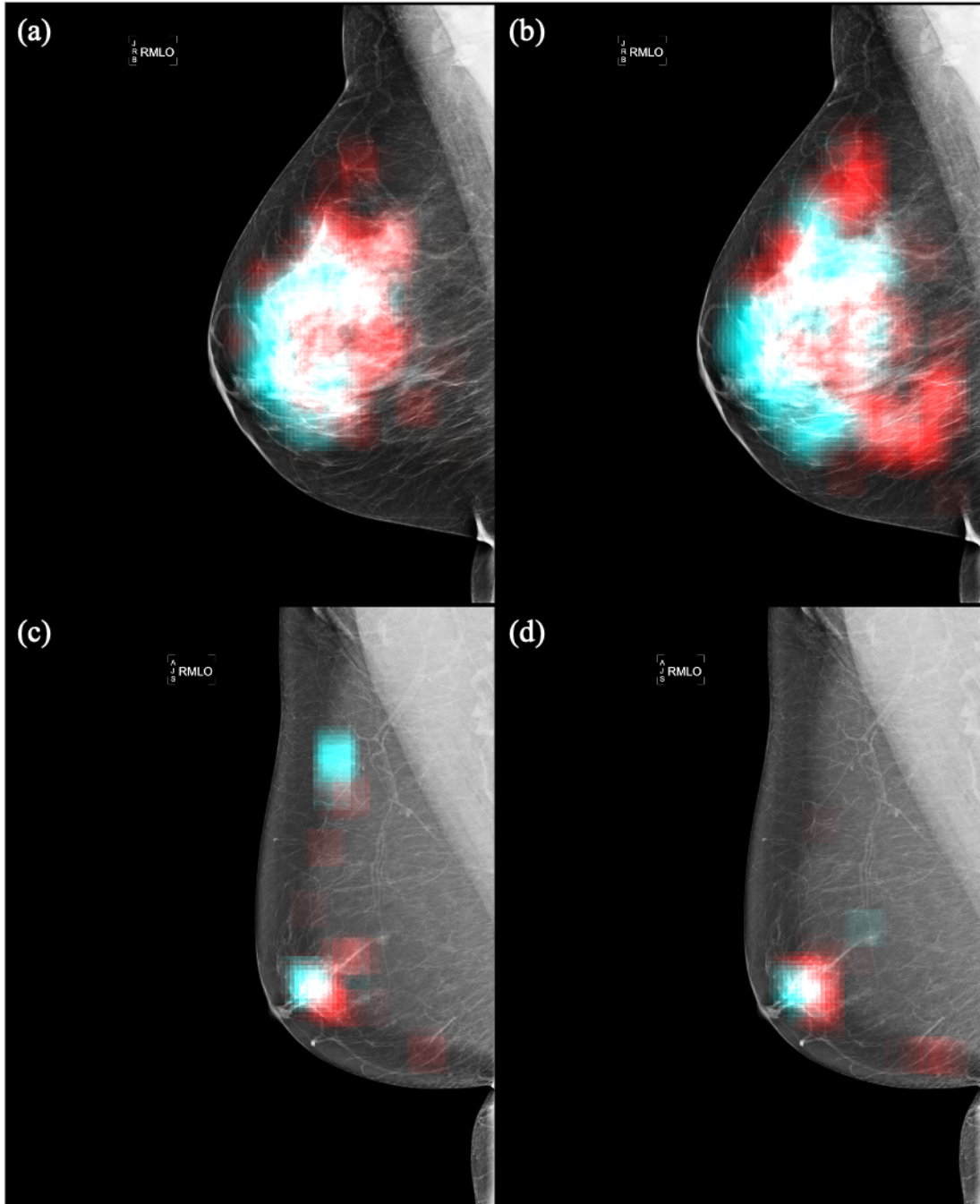
Figure 7.2: Visualization of risky (red) and healthy dense (cyan) mammographic tissue output from the 2D WTMM sliding window analysis using the Gaussian (ac) and Mexican hat (bd) smoothing functions. A cancerous (top row) and normal (bottom row) patient are seen here from the Maine mammographic dataset.

7.2 Future Research

The CompuMAINE Laboratory has recently been granted access to a set of longitudinal mammograms with a total of 9,300 benign, cancerous, and control patients from the OPTIMAM mammographic dataset [54]. To further validate the conclusions in this thesis, the 2D WTMM sliding window analysis with both Gaussian and Mexican hat smoothing functions will analyze the mammograms in the OPTIMAM dataset. The wavelet leaders methodology will also be implemented, as this methodology would allow for the entire grayscale mammogram to be analyzed via a texture based analysis rather than the sliding window analysis current embedded into the 2D WTMM approach [55, 56].

The application of the Wilcoxon rank-sum methodology in this thesis is applied only to MLO mammograms. The application of the Mexican hat smoothing function in the 2D WTMM sliding window analysis demonstrates a larger statistical difference in risky dense breast tissue for benign and cancerous CC mammograms in the Maine dataset (Table 7.1). With this, the incorporation of CC and MLO mammograms into the statistical analysis together will be examined to most accurately assess a patient's breast cancer risk through the 2D WTMM sliding window analysis. Finally, rather than iterating through various a_{min} and a_{max} values, the median a_{min} and a_{max} across all mammograms of a patient dataset will be implemented into the 2D WTMM sliding window analysis to examine how this affects the statistical comparison between benign and cancerous mammograms.

Table 7.1: The 2D WTMM sliding window analysis is tested on CC mammograms in the Maine dataset with the Gaussian and Mexican hat smoothing functions while varying $MinADelta$. The p-values seen here are output through the Wilcoxon rank-sum statistical test for the comparison of benign and cancerous mammograms. The greatest significant difference between benign and cancerous CC mammograms is seen through the Mexican hat smoothing function.

Gaussian			Mexican Hat			
Fatty Tissue	Risky Dense Tissue	Healthy Dense Tissue	Fatty Tissue	Risky Dense Tissue	Healthy Dense Tissue	$MinADelta$
0.19252	0.00175	0.02918	0.51745	2.00E-05	0.00369	1.0
0.18077	0.00088	0.02378	0.51745	2.00E-05	0.00424	1.5
0.08279	0.00287	0.03099	0.36168	9.00E-05	0.00533	2.0
0.03408	0.01368	0.0511	0.19685	0.00014	0.00924	2.5
0.01788	0.06091	0.05492	0.08602	0.00012	0.01948	3.0
0.01156	0.12173	0.06945	0.03651	0.00028	0.04179	3.5
0.01067	0.19067	0.1295	0.01817	0.00373	0.06689	4.0
0.02246	0.23585	0.1516	0.01391	0.02789	0.15957	4.5
0.09315	0.26194	0.1837	0.0147	0.21763	0.35562	4.9

REFERENCES

[1] Nicholas Chronis. Disparities in breast cancer mortality among african american women and recommended interventions.

[2] Ingrid Schreer. Dense breast tissue as an important risk factor for breast cancer and implications for early detection. *Breast Care*, 4(2):89–92, 2009.

[3] Patricia Fernández-Nogueira, Mario Mancino, Gemma Fuster, Paloma Bragado, Miquel Prats de Puig, Pere Gascón, Francisco Javier Casado, and Neus Carbó. Breast mammographic density: Stromal implications on breast cancer detection and therapy. *Journal of Clinical Medicine*, 9(3):776, 2020.

[4] Manju Bala Popli, Rahul Teotia, Meenakshi Narang, and Hare Krishna. Breast positioning during mammography: Mistakes to be avoided. *Breast Cancer: Basic and Clinical Research*, 8:119–124, 7 2014.

[5] Seung Ja Kim, Woo Kyung Moon, Min Hyun Seong, Nariya Cho, and Jung Min Chang. Computer-aided detection in digital mammography: false-positive marks and their reproducibility in negative mammograms. *Acta Radiologica*, 50(9):999–1004, 2009.

[6] Law Kumar Singh, Munish Khanna, and Rekha Singh. Artificial intelligence based medical decision support system for early and accurate breast cancer prediction. *Advances in Engineering Software*, 175:103338, 2023.

[7] Despina Kontos and Emily F Conant. Can ai help make screening mammography "lean"?, 2019.

[8] Timothy W Freer and Michael J Ulissey. Screening mammography with computer-aided detection: prospective study of 12,860 patients in a community breast center. *Radiology*, 220(3):781–786, 2001.

[9] Zach Marin, Kendra A Batchelder, Brian C Toner, Lyne Guimond, Evgeniya Gerasimova-Chechkina, Amy R Harrow, Alain Arneodo, and Andre Khalil. Mammographic evidence of microenvironment changes in tumorous breasts. *Medical physics*, 44(4):1324–1336, 2017.

[10] Evgeniya Gerasimova-Chechkina, Brian C Toner, Kendra A Batchelder, Basel White, Genrietta Freynd, Igor Antipev, Alain Arneodo, and Andre Khalil. Loss of mammographic tissue homeostasis in invasive lobular and ductal breast carcinomas vs. benign lesions. *Frontiers in physiology*, 12:660883, 2021.

[11] A Arneodo, NGRS Decoster, and SG 2 Roux. A wavelet-based method for multifractal image analysis. i. methodology and test applications on isotropic and anisotropic random rough surfaces. *The European Physical Journal B-Condensed Matter and Complex Systems*, 15:567–600, 2000.

[12] André Khalil, G Joncas, F Nekka, Pierre Kestener, and Alain Arnéodo. Morphological analysis of hi features. ii. wavelet-based multifractal formalism. *The Astrophysical Journal Supplement Series*, 165(2):512, 2006.

[13] Rebecca L Siegel, Kimberly D Miller, Nikita Sandeep Wagle, and Ahmedin Jemal. Cancer statistics, 2023. *CA: a cancer journal for clinicians*, 73(1):17–48, 2023.

[14] Eitan Amir, Orit C Freedman, Bostjan Seruga, and D Gareth Evans. Assessing women at high risk of breast cancer: a review of risk assessment models. *JNCI: Journal of the National Cancer Institute*, 102(10):680–691, 2010.

[15] Jessica A Cintolo-Gonzalez, Danielle Braun, Amanda L Blackford, Emanuele Mazzola, Ahmet Acar, Jennifer K Plichta, Molly Griffin, and Kevin S Hughes. Breast cancer risk models: a comprehensive overview of existing models, validation, and clinical applications. *Breast cancer research and treatment*, 164:263–284, 2017.

[16] Mitchell H Gail, Louise A Brinton, David P Byar, Donald K Corle, Sylvan B Green, Catherine Schairer, and John J Mulvihill. Projecting individualized probabilities of developing breast cancer for white females who are being examined annually. *JNCI: Journal of the National Cancer Institute*, 81(24):1879–1886, 1989.

[17] D Gareth R Evans and Anthony Howell. Breast cancer risk-assessment models. *Breast cancer research*, 9(5):1–8, 2007.

[18] Mitchell H Gail, Joseph P Costantino, David Pee, Melissa Bondy, Lisa Newman, Mano Selvan, Garnet L Anderson, Kathleen E Malone, Polly A Marchbanks, Worta McCaskill-Stevens, et al. Projecting individualized absolute invasive breast cancer risk in african american women. *Journal of the National Cancer Institute*, 99(23):1782–1792, 2007.

[19] Shayan Shaghayeq Nazari and Pinku Mukherjee. An overview of mammographic density and its association with breast cancer. *Breast cancer*, 25:259–267, 2018.

[20] Corinne Balleyguier, Salma Ayadi, Kim Van Nguyen, Daniel Vanel, Clarisse Dromain, and Robert Sigal. Birads™ classification in mammography. *European journal of radiology*, 61(2):192–194, 2007.

[21] Marcela G del Carmen, Elkan F Halpern, Daniel B Kopans, Beverly Moy, Richard H Moore, Paul E Goss, and Kevin S Hughes. Mammographic breast density and race. *American Journal of Roentgenology*, 188(4):1147–1150, 2007.

[22] Jinbo Chen, David Pee, Rajeev Ayyagari, Barry Graubard, Catherine Schairer, Celia Byrne, Jacques Benichou, and Mitchell H Gail. Projecting absolute invasive breast cancer risk in white women with a model that includes mammographic density. *Journal of the National Cancer Institute*, 98(17):1215–1226, 2006.

[23] Jeffrey A Tice, Steven R Cummings, Rebecca Smith-Bindman, Laura Ichikawa, William E Barlow, and Karla Kerlikowske. Using clinical factors and mammographic

breast density to estimate breast cancer risk: development and validation of a new predictive model. *Annals of internal medicine*, 148(5):337–347, 2008.

[24] Donna Shattuck-Eidens, Arnold Oliphant, Melody McClure, Celeste McBride, Jamila Gupte, Todd Rubano, Dmitry Pruss, Sean V Tavtigian, David H-F Teng, Nils Adey, et al. Brca1 sequence analysis in women at high risk for susceptibility mutations: risk factor analysis and implications for genetic testing. *Jama*, 278(15):1242–1250, 1997.

[25] Thomas S Frank, Susan A Manley, Olufunmilayo I Olopade, Shelly Cummings, Judy E Garber, Barbara Bernhardt, Karen Antman, Donna Russo, Marie E Wood, Lisa Mullineau, et al. Sequence analysis of brca1 and brca2: correlation of mutations with family history and ovarian cancer risk. *Journal of Clinical Oncology*, 16(7):2417–2425, 1998.

[26] Jeffrey N Weitzel, Veronica I Lagos, Carey A Cullinane, Patricia J Gambol, Julie O Culver, Kathleen R Blazer, Melanie R Palomares, Katrina J Lowstuter, and Deborah J MacDonald. Limited family structure and brca gene mutation status in single cases of breast cancer. *Jama*, 297(23):2587–2595, 2007.

[27] Noralane M Lindor, Kiley J Johnson, Hayden Harvey, V Shane Pankratz, Susan M Domchek, Katherine Hunt, Marcia Wilson, M Cathie Smith, and Fergus Couch. Predicting brca1 and brca2 gene mutation carriers: comparison of penn ii model to previous study. *Familial cancer*, 9:495–502, 2010.

[28] CA Gilpin, N Carson, and AGW Hunter. A preliminary validation of a family history assessment form to select women at risk for breast or ovarian cancer for referral to a genetics center. *Clinical genetics*, 58(4):299–308, 2000.

[29] Donald A Berry, Giovanni Parmigiani, Juana Sanchez, Joellen Schildkraut, and Eric Winer. Probability of carrying a mutation of breast-ovarian cancer gene brca1 based on family history. *Journal of the National Cancer Institute*, 89(3):227–237, 1997.

[30] Emanuele Mazzola, Amanda Blackford, Giovanni Parmigiani, and Swati Biswas. Recent enhancements to the genetic risk prediction model brcapro. *Cancer informatics*, 14:CIN–S17292, 2015.

[31] Antonis C Antoniou, Paul DP Pharoah, Greg McMullan, Nickolas E Day, MR Stratton, J Peto, BJ Ponder, and DF2746531 Easton. A comprehensive model for familial breast cancer incorporating brca1, brca2 and other genes. *British journal of cancer*, 86(1):76–83, 2002.

[32] Giovanni Parmigiani, Donald A Berry, and Omar Aguilar. Determining carrier probabilities for breast cancer–susceptibility genes brca1 and brca2. *The American Journal of Human Genetics*, 62(1):145–158, 1998.

[33] Andrew J Lee, Alex P Cunningham, KB Kuchenbaecker, N Mavaddat, Douglas F Easton, and Antonis C Antoniou. Boadicea breast cancer risk prediction model: updates to cancer incidences, tumour pathology and web interface. *British journal of cancer*, 110(2):535–545, 2014.

[34] Anne S Quante, Alice S Whittemore, Tom Shriver, Konstantin Strauch, and Mary B Terry. Breast cancer risk assessment across the risk continuum: genetic and nongenetic risk factors contributing to differential model performance. *Breast Cancer Research*, 14:1–12, 2012.

[35] Peter A Fasching, Mayada R Bani, Carolin Nestle-Krämling, Tim O Goecke, Dieter Niederacher, Matthias W Beckmann, and Michael P Lux. Evaluation of mathematical models for breast cancer risk assessment in routine clinical use. *European journal of cancer prevention*, pages 216–224, 2007.

[36] Adam R Brentnall, Elaine F Harkness, Susan M Astley, Louise S Donnelly, Paula Stavrinos, Sarah Sampson, Lynne Fox, Jamie C Sergeant, Michelle N Harvie, Mary Wilson, et al. Mammographic density adds accuracy to both the tyrer-cuzick and gail breast cancer risk models in a prospective uk screening cohort. *Breast Cancer Research*, 17:1–10, 2015.

[37] Jayashree Subramanian, Akila Karmegam, Elpiniki Papageorgiou, Nikolaos Papandrianos, and A Vasukie. An integrated breast cancer risk assessment and management model based on fuzzy cognitive maps. *Computer methods and programs in biomedicine*, 118(3):280–297, 2015.

[38] Debbie Overman. New research finds icad's profound ai risk for digital breast tomosynthesis is 2.4 x more accurate than traditional lifetime risk models. *AXIS Imaging News*, 2022.

[39] Keri Stephens. icad launches personalized risk assessment technology for 3d mammography. *AXIS Imaging News*, 2021.

[40] Benoit B Mandelbrot and Benoit B Mandelbrot. *The fractal geometry of nature*, volume 1. WH freeman New York, 1982.

[41] Heinz-Otto Peitgen and Dietmar Saupe. *The science of fractal images*. Springer-Verlag, 1988.

[42] Pierre Kestener, Jean Marc Lina, Philippe Saint-Jean, and Alain Arneodo. Wavelet-based multifractal formalism to assist in diagnosis in digitized mammograms. *Image Analysis & Stereology*, 20(3):169–174, 2001.

[43] Armin Bunde, Jürgen Kropp, Hans Joachim Schellnhuber, Alain Arneodo, Benjamin Audit, Nicolas Decoster, Jean-Francois Muzy, and Cedric Vaillant. Wavelet based multifractal formalism: applications to dna sequences, satellite images of the cloud structure, and stock market data. *The science of disasters: climate disruptions, heart attacks, and market crashes*, pages 26–102, 2002.

[44] N Decoster, SG Roux, and A Arneodo. A wavelet-based method for multifractal image analysis. ii. applications to synthetic multifractal rough surfaces. *The European Physical Journal B-Condensed Matter and Complex Systems*, 15(4):739–764, 2000.

[45] Stephane Mallat, Sifen Zhong, et al. Characterization of signals from multiscale edges. *IEEE Transactions on pattern analysis and machine intelligence*, 14(7):710–732, 1992.

[46] XC Jin, SH Ong, et al. A practical method for estimating fractal dimension. *Pattern Recognition Letters*, 16(5):457–464, 1995.

[47] Chinmaya Panigrahy, Ayan Seal, and Nihar Kumar Mahato. Image texture surface analysis using an improved differential box counting based fractal dimension. *Powder Technology*, 364:276–299, 2020.

[48] PHSW Kulatilake and J Um. Requirements for accurate quantification of self-affine roughness using the roughness–length method. *International Journal of Rock Mechanics and Mining Sciences*, 36(1):5–18, 1999.

[49] Ashutosh Chamoli, Abhey Ram Bansal, and VP Dimri. Wavelet and rescaled range approach for the hurst coefficient for short and long time series. *Computers & Geosciences*, 33(1):83–93, 2007.

[50] Carlos Parra, Khan Iftekharuddin, and David Rendon. Wavelet based estimation of the fractal dimension in fbm images. In *First International IEEE EMBS Conference on Neural Engineering, 2003. Conference Proceedings.*, pages 533–536. IEEE, 2003.

[51] Martin Dlask and Jaromir Kukal. Hurst exponent estimation of fractional surfaces for mammogram images analysis. *Physica A: Statistical Mechanics and its Applications*, 585:126424, 2022.

[52] Kendra A Batchelder, Aaron B Tanenbaum, Seth Albert, Lyne Guimond, Pierre Kestener, Alain Arneodo, and Andre Khalil. Wavelet-based 3d reconstruction of microcalcification clusters from two mammographic views: new evidence that fractal tumors are malignant and euclidean tumors are benign. *PloS one*, 9(9):e107580, 2014.

[53] A Khalil, C Aponte, R Zhang, T Davisson, I Dickey, D Engelman, M Hawkins, and M Mason. Image analysis of soft-tissue in-growth and attachment into highly porous alumina ceramic foam metals. *Medical engineering & physics*, 31(7):775–783, 2009.

[54] Mark D Halling-Brown, Lucy M Warren, Dominic Ward, Emma Lewis, Alistair Mackenzie, Matthew G Wallis, Louise S Wilkinson, Rosalind M Given-Wilson, Rita McAvinchey, and Kenneth C Young. Optimam mammography image database: a large-scale resource of mammography images and clinical data. *Radiology: Artificial Intelligence*, 3(1):e200103, 2020.

[55] Stéphane Jaffard, Bruno Lashermes, and Patrice Abry. Wavelet leaders in multifractal analysis. *Wavelet analysis and applications*, 1:219–264, 2006.

[56] Barbara Pascal, Nelly Pustelnik, and Patrice Abry. Strongly convex optimization for joint fractal feature estimation and texture segmentation. *Applied and Computational Harmonic Analysis*, 54:303–322, 2021.

BIOGRAPHY OF THE AUTHOR

Basel's mother's battle with breast cancer throughout high school led to his wish to conduct breast cancer research as a member of the CompuMAINE Laboratory under Professor Andre Khalil. He graduated magna cum laude in May of 2022 with a bachelors of science in biomedical engineering and a minor in Mathematics from The University of Maine. In addition, he graduated with highest honors with the defense of his Honor's thesis titled, *Wavelet-Based Automatic Breast Segmentation for Mammograms.* Basel will begin a PhD program in Biomedical Engineering at Brown University as a member of The Dawson Lab in Fall 2023.

LinkedIn Profile: https://www.linkedin.com/in/basel-white-620203173/

He is a candidate for the Master of Science degree in Biomedical Engineering from the University of Maine in May 2023.